

# Proximal Hydrothermal Alteration of the Carrapateena Deposit

Thesis submitted in accordance with the requirements of the University of Adelaide for an  
Honours Degree in Geology

Josiah Park

October 2021



THE UNIVERSITY  
*of* ADELAIDE



## **HYDROTHERMAL ALTERATION OF CARRAPATEENA**

### **ABSTRACT**

Carrapateena is an IOCG (Iron Oxide Copper Gold) deposit, located west of Lake Torrens on the Eastern edge of the Gawler Craton. This deposit is located on the Stuart Shelf and is hosted by the 1850Ma Donington Suite granite. Carrapateena is a magmatic system controlled by fault structures and is compositionally impacted by hydrothermal alteration. The deposit partially is a magnetite orebody which is associated with chlorite alteration, while the top 1.5km of the deposit is predominately altered by hematite, with potassic and hydrolytic alteration. However, limited research on the host granite and alteration textures has been completed for this deposit. Investigation into the hydrolytic altered portion of the ore-system and granite surrounding, is made to determine the geochemical, mineralogical, and timing of the Carrapateena deposit hydrothermal event history.

Mineral textures between granite and hydrothermal minerals show the extent of the hydrolytic alteration through the granite. Typical alteration minerals in the host granite are hydrous forms of altered mica and feldspar, combining their textures with trace element signatures of monazite, xenotime, and apatite, findings provide insight into the hydrothermal history of the Carrapateena host granite, the Donington Suite. The geochronology associated with these minerals describe hydrothermal events predating the ore system and confirms the associated age for host granite surrounding the deposit.

### **KEYWORDS**

**IOCG, Hydrothermal, Alteration, Granite, Monazite, Apatite.**



**TABLE OF CONTENTS**

HYDROTHERMAL ALTERATION OF CARRAPATEENA ..... i

1. INTRODUCTION..... 3

2. GEOLOGICAL BACKGROUND..... 8

2.1 Regional Geology ..... 8

2.2 Deposit Geology ..... 10

2.3 Alteration Mineralogy ..... 12

3. METHODS ..... 16

3.1 Sample Collection..... 16

3.2 Data Preparation ..... 17

3.3 Petrology..... 19

3.4 Scanning Electron Microscope (Hitachi 3800) ..... 19

3.5 Tornado microXRF..... 20

3.6 Laser Ablation Inductively Coupled Plasma Mass Spectrometry ..... 20

3.7 Geochronology Processing ..... 22

4. RESULTS..... 24

4.1 Petrology (Axioscan & M4 Tornado Micro XRF)..... 24

4.2 SEM & AMICS ..... 26

4.3 Tornado..... 31

4.4 Whole Rock Geochemistry..... 32

4.5 LA-ICP MS Geochronology..... 36

4.5.1 Apatite Geochronology & REE Chemistry..... 36

4.5.2 Monazite Geochronology & REE Chemistry ..... 38

4.5.3 Xenotime geochronology & REE chemistry ..... 40

4.5.4 Zircon Geochronology & REE chemistry ..... 42

5. DISCUSSION ..... 44

5.1 Mineralogical relationships and textures described in petrology ..... 44

5.2 Interpretation of U–Pb geochronology and trace elements ..... 45

5.3 Geochemical ..... 50

6. CONCLUSIONS ..... 54

7. Further study..... 55

## LIST OF FIGURES AND TABLES

### FIGURES

Figure 1. South Australian IOCG locations and alteration framework .....	6
Figure 2. Schematic diagram for study drillholes.....	7
Figure 3. Granite core samples from CAR2038.....	13
Figure 4. Sample intervals of targeted geochemical variation. ....	17
Figure 5. Axioscan XPL photomicrographs of 1.6m depth sample .....	25
Figure 6. Axioscan XPL photomicrographs of 700m depth sample. ....	26
Figure 7. Back Scattered Electron image (Hitachi 3800) of 1.6m Sample .....	27
Figure 8. Hitachi SEM 3800 granite 1” rock mount work .....	29
Figure 9. Hitachi SEM 3800 ore-zone/CBC 1” rock mount work, .....	30
Figure 10. Micro XRF image taken on m4 Tornado machine.....	32
Figure 11. Geochemical plots from CAR2038 bulk rock assay data .....	34
Figure 12. Alkali element concentration (Na/K) of CAR2038 and distal drillholes.....	35
Figure 13. Apatite Terra-wasserburg plots .....	37
Figure 14. CAR2038 monazite Wetherill and REE plots.....	39
Figure 15. CAR2038 xenotime Wetherill and REE plots .....	41
Figure 16. CAR2038 zircon Wetherill and REE plots .....	43
Figure 17. Time-space plot for geochronology across IOCGs on the Stuart Shelf.....	48
Figure 18. Affect of common lead and modern lead loss in xenotime.....	50
Figure 19. Alkali element Plot Na:K, for CAR2038 compared to Olympic Dam. ....	51
Figure 20. Apatite REE chemistry comparison with CBC varied samples.....	53

### TABLES

Table 1. Bureau Veritas labcodes for bulk rock analysis on geochemistry.....	18
Table 2. Specifications/details for laser ablation ICP MS.....	21
Table 3. Geochronolgy standards from literature compared to analyses in this study...	23

## 1. INTRODUCTION

OZ Minerals' Carrapateena Iron Oxide Copper-Gold (IOCG) deposit is located 160km North of Port Augusta, on the eastern margin of the Gawler Craton in South Australia (Figure 1a), and is part of the Olympic Copper-Gold Province (Skirrow et al. 2019). The Carrapateena deposit is classified as a hematite-breccia endmember IOCG (Williams et al., 2005.), and has a resource of 970 Mt of 0.5% copper, 0.2 g/t gold and 3 g/t silver with a predicted mine life of at least 20 years (OZ Minerals).

Economic mineralisation within the deposit is located in the sub-vertical, Carrapateena Breccia Complex (CBC) (Figure 2), which is comprised of polymictic hematite-granite breccia and hosted by the surrounding Donington Suite granite (~1850Ma, Mortimer et al., 1988).

Copper (Cu) mineralisation is present as the Cu sulphides chalcopyrite and bornite, as well as minor chalcocite and a variety of secondary Cu-bearing minerals formed by the redistribution of these primary minerals (Sawyer 2014). The CBC is proposed to have formed related to the intrusion of the Hiltaba Magmatic Suite (1595-1575Ma) (Chapman et al. 2019). However, the history of hydrothermal events which resulted in the formation of the Carrapateena deposit has had very limited investigation.

Paragenesis for the deposit can be separated into diagenetic and post diagenetic event sequences (Taylor 2014). The sequence investigated in this study relates to the post-diagenetic sequence (Taylor 2014), reported to be an early magnetite pyrite stage, followed by hematite, then Cu sulphides and then hydrothermal breccia development. With the ore system supported by hematite, and magnetite associated to the basement

(Vella 2009), the deposit is interpreted to have formed as hydrothermal fluids moved through and overprinted magnetite (Taylor 2014). The geochemical expression of associated hydrothermal alteration on the deposit and surrounding host rock are currently poorly characterised.

Typical calc-alkaline magma source IOCG deposits are differentiated based on their distance from the magma source, these classifications are Iron Skarn-type, Kiruna-type, Olympic Dam-type and Cloncurry-type, from source-proximal to distal respectively (Corriveau 2019). The Carrapateena deposit is most similar to an Olympic-Dam style IOCG, based on the hematite matrix and predominant brecciation. This style of IOCG has alteration textures described by (Hitzman 1992), where deeper portions of these systems exhibit sodic alteration, contain albite magnetite and actinolite or chlorite, and generally lack quartz. Igneous feldspars are the first minerals to be altered after micas, followed by fine-grained groundmass material and mafic minerals. Sodic alteration underlies potassic alteration and in some areas potassic alteration is overlain by sericite/hydrolytic alteration, (Figure 1b). Alteration types describe the extent of magnetite stockwork for these deposits, where hematite is at the top of the system in the sericite/hydrolytic altered area. This would put the Carrapateena ~1,500m deposit ore zone in predominantly hydrolytic-potassic alteration with interpreted sodic alteration at depth.

Given the size of the Carrapateena deposit, and the scope of an honours project, it is unfeasible to describe alteration on both the ore-system and surrounding host rock to a comprehensive extent. This study aims to investigate hydrothermal alteration proximal

to the Carrapateena deposit, through investigation of textural relationships, geochemistry, and in-situ geochronology of one drillhole. This will be achieved using samples collected at varying distances from the deposit, which will provide information on the intensity and nature of hydrothermal alteration which has affected the host granite away from the deposit (Figure 2a). Furthermore, an in-depth study on the drill hole which intersects the deposit and will be analysed through geochemistry and petrography, (Figure 2b).

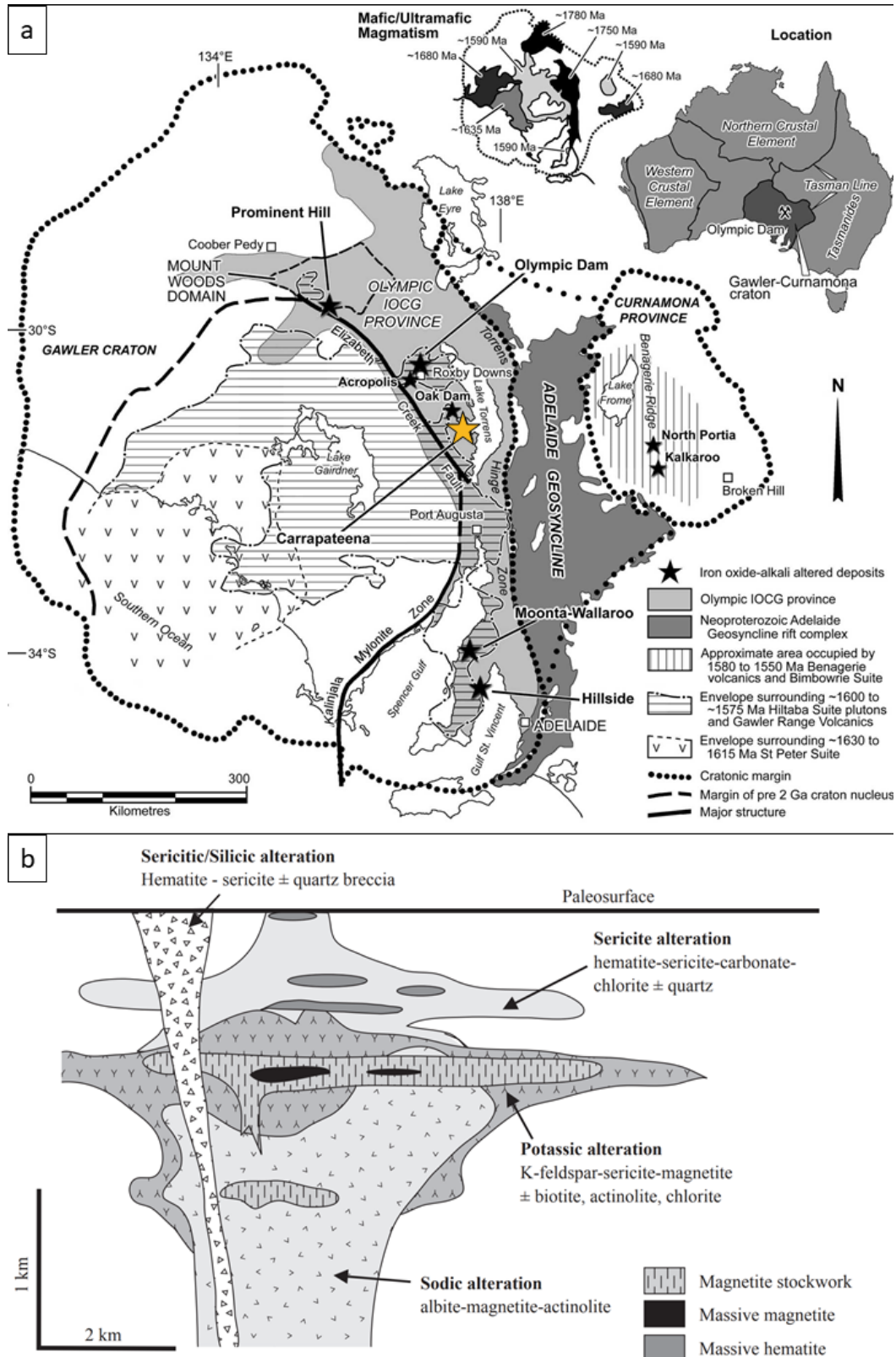


Figure 1. (a) South Australian province map, focused on the Galwer-Curnamona craton, starred with locations of major IOCG deposits, Carrapateena starred in yellow, (Porter 2010). (b) Theoretical genetic model for alteration zoning related to IOCG development (Hitzman 1992).

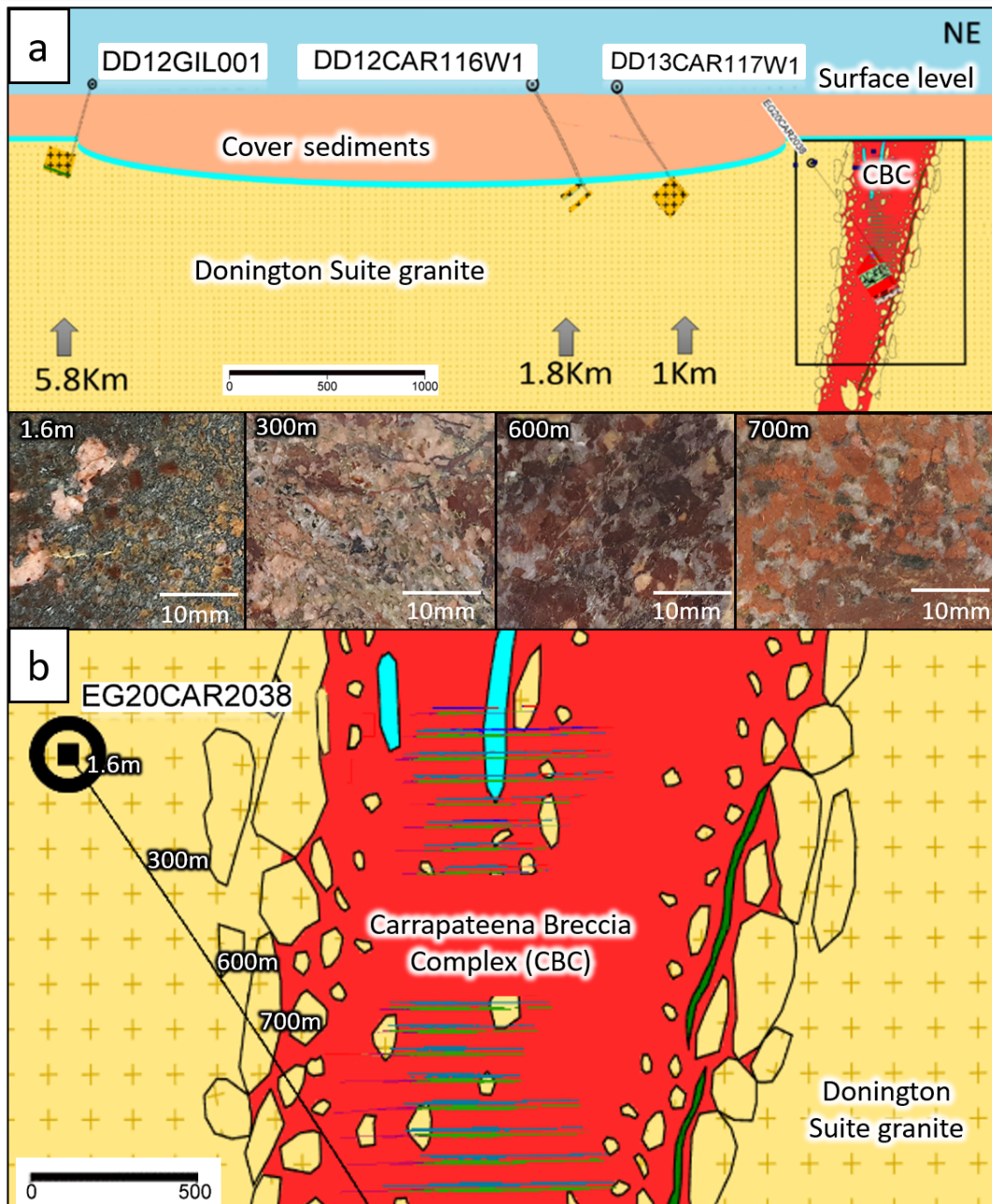


Figure 2. Schematic diagram for study drillholes, data from OZ Minerals, exported using Micromine 2018. Red area is the Carrapateena Breccia Complex (CBC), yellow crossed lithology is Donington Suite granite hostrock. Cyan-blue is unconforming basal conglomerate, seen in rafts in the CBC. Beige 'cover sequence' is comprised of Neoproterozoic sediments-Woomera Shale, Corraberra Sandstone, and Arcoona Quartzite. Green shapes inside the CBC are dykes. (a) distal drillhole data is to be assessed into the host granite, where drill holes up to 5.8km distal from the deposit are used to build understanding of the most unaltered host granite. (b) Drillhole-CAR2038 (collared underground along the decline), sample intervals seen above as photographs at 1.6m, 300m, 600m and 700m for petrographic analysis and U-Pb in-situ geochronology.

## **2. GEOLOGICAL BACKGROUND**

The Carrapateena IOCG deposit is hosted in the Donington Suite granite, with a cover sequence of about 500m of sediment (Figure 2a), found on the western edge of the modern-day Lake Torrens (Figure 3a).

### **2.1 Regional Geology**

The geology of the Gawler Craton is comprised of a Meso-Neoproterozoic core surrounded by Paleoproterozoic to Mesoproterozoic rocks. Tectonic activity caused late Archean basin development between 2560-2500 Ma, and collisional deformation through the 2480-2420Ma Sleafordian orogeny (Reid and Hand 2012). Theorised IOCG related magmatism is interpreted to be Hiltaba Suite granites (1595-1575 Ma Chapman et al 2019) and the coeval Gawler Range Volcanics (GRV). These units have been suggested to have interacted with Wallaroo Group (1750Ma) meta-sediments which retained some formation water (Fabris and Reid 2015), allowing for igneous and sedimentary sourced fluid mixing, which provided suitable water chemistry for IOCG generation and subsequently hydrothermally impacting the surrounding granite.

The oldest known unit is the Cooyerdoo granite (3.1Ga Fraser et al 2010). Followed by units related to the Sleaford and Mulgathing complexes (2550Ma-2500Ma Archean, Swain et al., 2005) composed of felsic and mafic volcanics. The next stage is the protoliths to the Mitalie Gneiss (2000Ma Curtis et al 2017), the Hutchinson Group follows, rich in carbonates quartzites and dolomite (2000-1690 Ma, Parker and Lemon, 1982), with the Myola volcanics and associated Broadview schist (Reid and Hand 2012), and McGregor volcanics (1755Ma Curtis and Ried 2017). The Donington Suite I-type metaluminous granodiorites (Curtis 2019) intruded the eastern margin of the



craton (1850Ma, Mortimer et al., 1988). Donington magmatism has been interpreted to be related to subduction under the eastern margin of the Olympic domain (Betts and Giles, 2006; Ferris et al., 2002). Extensional basins formed between 1790 and 1740Ma, accommodating the Wallaroo Group, including intrusive and extrusive felsic and mafic rocks, associated to rifting/extensional basins, with carbonates and clastic sediments (Cowley et al., 2003; Reid, 2019). Tectonic activity interpreted as the Kimban Orogeny (1730-1690 Ma) resulted in the northeast-trending Kalinjala shear zone along the Hutchinson Group and Donington Suite (Hand et al., 2007). Following the Kimban orogeny, is the extensive St Peters Suite with ages ranging from 1633 Ma to 1608 Ma (Reid et al 2016). Late Paleoproterozoic- early Mesoproterozoic GRV and Hiltaba Suite magmatics (1630-1500Ma, Daly et al 1998) intruded, with deformation of the Hiltaba Suite-felsic magmatism seen in northwest-southeast trending ductile shearing structures associated to the Kararan Orogeny (1570-1555 Payne et al 2008). The Warrina Supergroup (840-710Ma Priess, 2000) (Callana and Burra Groups), Heysen Supergroup (700-500 Ma Priess, 2000)(Umberatana and Wilpena Group), Moralana Supergroup (530-515Ma Priess, 2000)(Cambrian sediments) successively followed, to cover the older lithologies. The Heysen and Moralana Supergroups blanket the entire northern Olympic Domain (Hall et al 2018).

The Gawler Craton has been surveyed by aero-magnetic and gravity geophysical methods, where the expression of IOCG deposits can be seen superimposed on older geological features as significant density and magnetic anomalies. Carrapateena is located on the southwest edge of a larger magnetic anomaly, associated with a gravity high and a distinct magnetic anomaly (Vella et al 2012). Anomalous density and magnetic responses are attributed to the hematite/magnetite ore in the deposit, being

denser and with a magnetic field that differs from the background granite composition. This combination of partially overlapping geophysical anomalies was instrumental in driving the exploration for this covered deposit.

## **2.2 Deposit Geology**

The Carrapateena deposit is hosted by the 1850 Ma Donington Suite granite with hematite ore-breccia bordered by faults. Copper, gold and rare earth elements (REEs) mineralisation are hosted within the CBC which underlies the ~500m of cover sediment sequence. Structurally, the deposit is a hematite breccia 'pipe-like' system, where rafts and fragments of host granite and small quantities sedimentary volcanogenic breccia are irregularly distributed within a hematite breccia (Taylor 2014).

The intense alteration and fragmentation of the deposit has hindered concise paragenetic interpretation. Features from interpreted early-paragenesis are described by Roger Taylor as sericite and chlorite which predated an initial mineralisation stage of magnetite pyrite and chalcopyrite. The early stages are altered by a major hydrothermal brecciation, associated to a second stage of mineralisation with hematite, chalcopyrite, bornite, pyrite and gold. Late stage paragenesis is seen as veining Cu sulphides and carbonates (Taylor 2014), with complex alteration of host granite surrounding the deposit related to the major hydrothermal intrusive brecciation (Taylor 2014).

Further aspects of interpreted paragenesis are based on multiple phases of ore generation, where early magnetite formed in the deposit is later replaced by hematite (Sawyer 2014).

The key resource in the deposit is broadly characterised around three zones, the Bornite Zone, Chalcopyrite Zone, and Barren Zone. The Bornite Zone is defined by a Cu/S ratio that indicates bornite is the dominant Cu sulphide. The Chalcopyrite Zone contains some bornite, but chalcopyrite is the dominant sulphide. The Barren Zone contains trace amounts of Cu (<100ppm) and is abundant in earthy hematite alteration (Sawyer 2018). Cu sulphides - bornite and chalcopyrite are interpreted to have formed at least in part by the replacement of the early pyrite/open space infill (Porter, 2010; Sawyer et al., 2017). The reported age of initial phase of sulphides has been reported as 1598 Ma using the Re-Os dating method, on pyrite and pyrite bearing hematite breccia (Sawyer et al, 2017). The deposit is also enriched in REE, mostly light rare earth elements (LREE), which is typical of IOCG deposits (Hitzman et al., 1992; Sawyer et al., 2014; Williams, 2012). REE are hosted in minerals such as monazite, apatite and xenotime which will preserve a characteristic REE signature and can differ from the surrounding host rock as some elements are able to react with fluids moving past them.

REE are transported in the Olympic Province by primarily REE-Cl species, deposited under conditions of suppressed REE-Cl activity (Krneta 2017). The timing of some REE minerals, monazite and xenotime, is linked to early stages of Cu-mineralisation (North 2020), allowing for further investigation of paragenesis of hydrothermal activity within the deposit through U-Pb dating.

### **2.3 Alteration Mineralogy**

Alteration in IOCGs is described on two scales, at deposit scale (inside the resource area) where descriptions are used to define the chemical and physical conditions in which the ore/ore-related lithologies have formed, and a district scale (100ms to kms), where descriptions can be made to characterise how the host rock has been affected by ore-forming events or other events such as regional heating from intrusive granites.

When discussing district scales, the term alteration halo is used to define a radial area that is interpreted as affected host rock and has retained some change imposed by the deposit forming events. For Carrapateena, the ore and breccia minerals are predominantly affected by hydrothermal fluids, which alter the host granite directly adjacent to the deposit and along any fracture and fluid pathways, forming more hydrous minerals such as chlorite and sericite.

Regional alteration on the Stuart Shelf affects up to hundreds of kilometres of the Donington Suite granite, with chloritization seen at places such as Olympic Dam and Wirrda Well, suggesting that low grade alteration has impacted large areas across the region (Courtney-Davies et al 2019). The Carrapateena deposit also exhibits chloritization at kilometre scale distances, with textures similar to that in Figure 3(a), where chlorite and the original biotite are seen together (Taylor 2014).

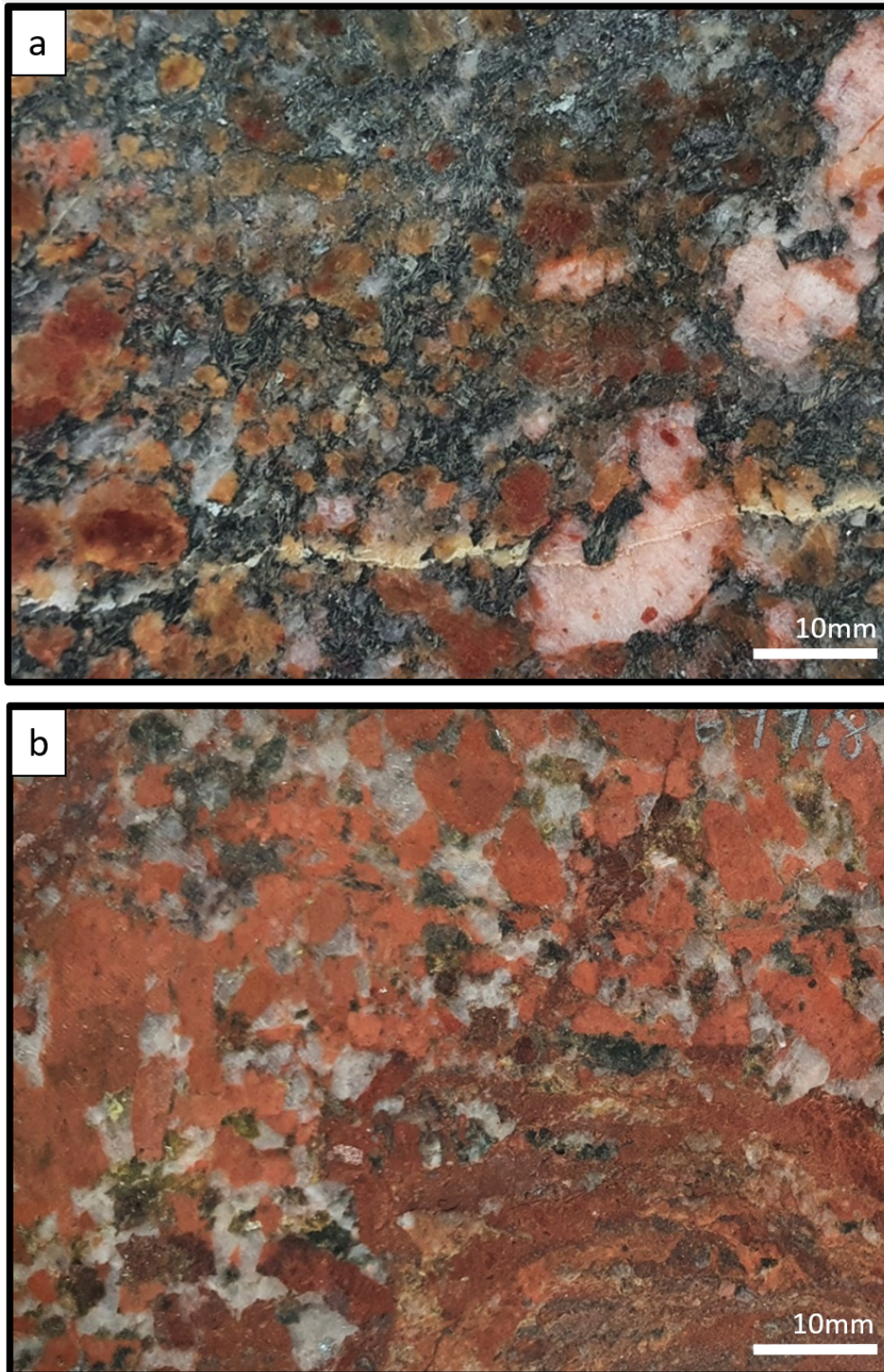


**Figure 3. Granite core samples from CAR2038, drillhole collared 500m underground, (a) sample from 1.6m drillhole depth, most distal sample from the CBC, quartz and feldspar phenocrysts surrounded by chlorite and biotite, with minor calcite veining. (b) 700m drillhole depth, CBC proximal, in breccia zone before hematite ore, quartz phenocrysts and feldspars being replaced by hematite, sericite remnants with veining hematite.**

Minerals within the CBC exhibit two major alteration assemblage types, hematite & white mica  $\pm$  quartz (orebody), and chlorite  $\pm$  hematite with sericite (halo), (Sawyer et al 2017), these two assemblages are commonly separate but do occur together. The alteration affecting the granite at the top of the deposit (500m depth from surface), is hematite and white-mica dominant. Chlorite increases with depth, passed the >1.5km of mineralised deposit (AusIMM 2017). Donington Suite granite at ~400m distance from the CBC has a chlorite dominant alteration, (Figure 3a). Adjacent to the CBC, hematite and sericite dominant alteration occurs, (Figure 3b).

Within the CBC rafts of granite are mostly altered by hematite, white mica and chlorite, hematite is dominant as it physically and chemically replaces granite, ranging from replacement features to being infill minerals in breccias, and occurring as massive hematite in the Barren Zone. The CBC hosts colloform textures of hematite suggesting the replacement of carbonates (Sawyer 2014). Increasing hematite is accompanied by increasing alteration of feldspars to white mica (sericite).

Alteration of granite both as rafts and as the surrounding host rock, affects minerals predictably, where biotite is the first mineral phase to begin hydrous reactions to form chlorite, followed by feldspars which react to form components of sericite. Within the deposit, plagioclase is absent, but K-feldspar may still persist in rafts of granite, with geochemical indication that Na within the host granite was removed, but K persists (dominantly in sericite). In zones of intense hematite alteration, both feldspars are absent, the brecciation of feldspars may have broken them down to smaller sizes and now may exist as micro-inclusions in the hematite. Magnetite is only recorded at large

depths >1.5km depth in the CBC (Nuemann et al 2019). Where the magnetite is present, chlorite is typically associated, along with pyrite and chalcopyrite (M. Nuemann pers. communication).

### **3. METHODS**

The aim of the methods that follow was to acquire a representative transition from the Donington Suite host granite to the CBC, through a combination of geochemistry, mineralogy, and geochronology. The focus on all methods is to investigate mineral change as a function of distance from the Carrapateena deposit, with investigation into the timing of alteration events.

#### **3.1 Sample Collection**

To acquire samples used in this work, field work at Carrapateena was completed from the 12<sup>th</sup>-16<sup>th</sup> of March 2021. The samples collected represent a distal to proximal relationship for minerals in the ore system and surrounding granite, seen in Figure 4. Samples were collected from drillhole CAR2038, a hole collared underground, which transects ~700m of host granite before intersecting the Bornite Zone, then the Chalcopyrite Zone. Whole-rock geochemical analysis of the drill holes, provided by OZ Minerals, was used to select suitable intervals of significant geochemical variation, which were then targeted for sampling. Within the ore zones, element intervals of elevated Ce and P were selected to improve the chances of sampling monazite. For samples of granite surrounding the ore zone, the geochemistry was made available after sampling 50m intervals (1m-750m depth), by selecting representative core to send for bulk-rock analysis. Areas of significant geochemical variation, or areas recording strong changes in geochemistry, were targeted for sub-sampling and used for rock mount work and thin sections, these being found at 1.6m, 300m, 600m and 700m depth in CAR2038, (Figure 4).



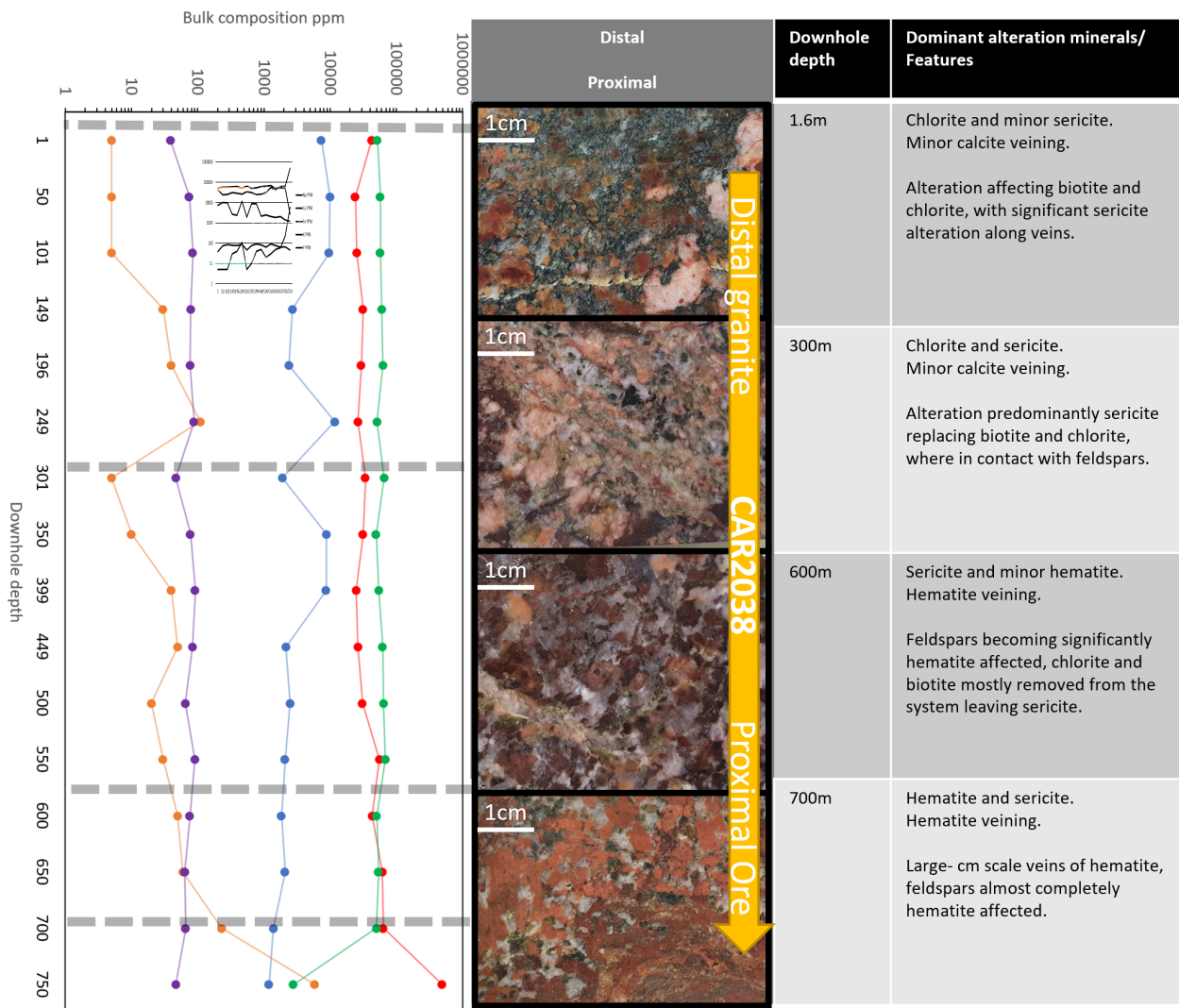


**Figure 4. Sample intervals of targeted geochemical variation, (1.6, 300, 600, 700m) with alteration texture descriptions. Bulk rock geochemistry for major elements in CAR2038 seen left, correlated to samples with hand sample descriptions right.**

### 3.2 Data Preparation

Whole rock and trace element geochemical data for OZ Minerals drillholes was generated by Bureau Veritas using methods with associated lab codes (Table 1). New geochemistry completed for this report (Figure 4), along with geochemistry obtained from mine operations was utilised in geochemical plots for this report. Sampling within the CAR2038 drillhole is conducted on half-core, with averaged compositions for every metre of hematite ore breccia, and in granite sampling was nominated by this study to

be every 50 metres. Bulk rock geochemical data was modelled using ioGAS (6.1, Reflex 2016) software and was spatially associated to the deposit using Micromine 2018.

**Table 1. Bureau Veritas lab codes for bulk rock analysis on geochemistry, with detection limits.**

<b>Lab Code</b>	<b>Method</b>	<b>Analytes (detection limit in ppm)</b>
<b>FA001</b>	Fire Assay (40 g), AAS finish	Au (0.01)
<b>LB101</b>	Lithium borate fusion, multi-acid digest, ICP-OES	Al (100), Ba (1), Ca (50), Cr (5), Fe (100), K (50), Mg (50), Mn (20), Na (50), P (100), Sc (2), Si (100), Ti (50), V (5), Zr (5)
<b>LB102</b>	Lithium borate fusion, multi-acid digest, ICP-MS	Ce (1), Dy (0.5), Er (1), Eu (0.5), Ga (1), Gd (1), Hf (0.5), Ho (1), In (0.5), La (1), Lu (0.5), Nd (1), Pr (0.5), Rb (0.5), Sm (1), Sn (5), Tb (0.5), Th (0.5), Tm (0.5), U (0.5), W (3), Y (1), Yb (1)
<b>MA201</b>	Modified aqua regia digest, ICP-OES	Cu (10), Ni (10), Pb (10), S (50), Zn (10)
<b>MA202</b>	Modified aqua regia digest, ICP-MS	Ag (0.2), As (2), Bi (0.1), Cd (0.1), Co (0.2), Cs (0.1), Mo (1), Nb (0.5), Sb (0.5), Se (2), Ta (0.1), Te (0.2)
<b>LB103</b>	Lithium Borate Fusion, Leach, Selective Ion Electrode	F (50)

### **3.3 Petrology**

Initial petrology was completed using an Olympus BX51 microscope, with DP21 digital camera. Reflected light petrology was conducted on polished rock mounts prepared for geochronology and trace-element work, while textural relations were investigated using thin sections. Thin sections were made by Adelaide Petrographics. The slide scanning imaging tool Axioscan was used to generate thin section cross-polarised light (XPL) and plane polarised light (PPL) images for each granite sample (Appendix B).

### **3.4 Scanning Electron Microscope (Hitachi 3800)**

Back scattered electron (BSE) images and automated mineralogy maps were created with the use of the Hitachi 3800 SEM. All images taken at a beam energy of 25kV at a standard working distance of 10mm. Automated mineralogy investigation characterisation software (AMICS) used to assess the surface area and spatial relation of minerals in polished rock mounts.

BSE images were taken for high resolution textures between target minerals, textures of altered crystals and the positioning of datable minerals, zircon, monazite xenotime and apatite. Cathodoluminescence images taken of zircon grains to identify zonation (Appendix C).

### **3.5 Tornado microXRF**

For further analysis into how the chemical composition of mineral phases changed along the drillhole CAR2038, Tornado XRF (X-Ray Fluorescence) at Adelaide Microscopy, University of Adelaide was used to map the relative enrichments of single elements, these were generated for Al, Ca, Cl, Fe, K, Mg, Mn, Na, P, S, Si, Sr, Ti, and Y (Appendix D). Exported images from Bruker software on the Tornado XRF are monochrome colour maps of individual elements, to overlay colours for better textural understanding, ImageJ (Schneider 2012) was used to merge colour channels.

### **3.6 Laser Ablation Inductively Coupled Plasma Mass Spectrometry (LA-ICP-MS)**

LA-ICP-MS was used on the samples containing datable elements and for obtaining trace element constraints on the veining of the host granite, using the Agilent 7900x in conjunction with the RESolution LR 193nm Excimer laser system at Adelaide Microscopy. The trace element data obtained allowed for isotope- U-Pb geochronology, following the methods of Payne et al., 2008; Fletcher et al., 2004; Thomson et al., 2012 for zircon, monazite, xenotime and apatite, respectively.

The processing of LA-ICP-MS data followed methodology (Appendix A) with specifications constrained by Table 2.

**Table 2. Specifications/details for LA-ICP-MS, Adelaide Microscopy, (Gilbert 2021).**

<b>LA-ICP-MS</b>				
Mineral:	Apatite	Monazite	Xenotime	Zircon
Brand/Model	Agilent 7900x ICP-MS			
Laser Wavelength	193 nm			
Beam size	30µm	20µm	13µm	20µm
Data acquisition	Time resolved analysis protocol			
Scanned Masses (dwell times, ms)	<sup>29</sup> Si (5), <sup>31</sup> P (5), <sup>35</sup> Cl (5), <sup>43</sup> Ca (5), <sup>51</sup> V (10), <sup>55</sup> Mn (10), <sup>57</sup> Fe (5), <sup>65</sup> Cu (5), <sup>88</sup> Sr (10), <sup>89</sup> Y (10), <sup>90</sup> Zr (10), <sup>139</sup> La (10), <sup>140</sup> Ce (10), <sup>141</sup> Pr (10), <sup>146</sup> Nd (10), <sup>147</sup> Sm (10), <sup>153</sup> Eu (10), <sup>157</sup> Gd (10), <sup>159</sup> Tb (10), <sup>163</sup> Dy (10), <sup>165</sup> Ho (10), <sup>166</sup> Er (10), <sup>169</sup> Tm (10), <sup>172</sup> Yb (10), <sup>175</sup> Lu (10), <sup>178</sup> Hf (10), <sup>201</sup> Hg (5), <sup>204</sup> Pb (10), <sup>206</sup> P (100), <sup>207</sup> Pb (100), <sup>208</sup> Pb (10), <sup>232</sup> Th (20), <sup>238</sup> U (20).			
Frequency	5Hz			
Fluence	3.5 J/cm <sup>-2</sup>	2 J/cm <sup>-2</sup>	2 J/cm <sup>-2</sup>	2 J/cm <sup>-2</sup>
Background collection (s)	30s			
Ablation (s)	30s			
Washout (s)	20s			
<b>ICP-MS Standardisation and Reduction</b>				
Mineral	Apatite	Monazite	Xenotime	Zircon
Primary Standard	MAD, NIST610	Madel, NIST610	BS-1, NIST610	GJ, NIST610
Secondary Standards	401, McClure	222, Ambat	MG-1, NIST610	91500, Plesovice
Computation	Iolite, IsoplotR	Iolite, IsoplotR	Iolite, IsoplotR	Iolite, IsoplotR

### **3.7 LA-ICP-MS U-Pb and trace element data processing**

Processing of LA-ICP MS data was done using iolite (Hellstrom, Paton et al 2011) for the reduction of U-Pb data. Reduction of geochronology data, U/Pb isotopic reduction and trace element analysis was completed following Appendix E.

IsoplotR (Vermeesch, 2018) was used to construct Tera-Wasserburg plots for apatite, and Wetherill Concordia plots for monazite, zircon and xenotime, and to produce  $^{207}\text{Pb}/^{206}\text{Pb}$  weighted mean age plots for concordant data. Verification of results completed using reference materials listed in Table 2. Standards gave ages within reported error margins from each of the related sources in Table 3.

**Table 3. LA ICP-MS standards from literature compared to analyses in this study, with number of analyses (n=).**

Primary Standards						1st analyses			2nd analyses		
Name	Reference	Mineral	Reported 206/238			Age from this study			Age from this study		
			Ma	+/-	n=	Ma	+/-	n=	Ma	+/-	n=
MAD	Thomson et al., 2012, G3	apatite	474.25	0.41	24	474.2	3.1	30	474.5	6.1	
MAdel	Payne et al., 2008, AJES	monazite	517.9	2.6	15	517.7	1.6	30	517.6	3.8	
BS-1	Fletcher et al., 2004, Chemical Geology	xenotime	508.9	0.3	10	509.02	4.6	-	-	-	
GJ	Jackson et al. 2004 Chem Geol 211, 47-69	zircon	600.7	1.1	20	602.5	2.2	-	-	-	
Secondary Standards						1st analyses			2nd analyses		
Name	Reference	Mineral	Reported 206/238			Age from this study			Age from this study		
			Ma	+/-	n=	Ma	+/-	n=	Ma	+/-	n=
401	Jay Thomson et al., 2016, JAAS	apatite	530.3	1.5	24	542.6	8.8	30	534	10	
McClure	Schoene and Bowring, 2006, CMP	apatite	523.51	1.47	24	534.7	14	30	548	35	
222	Adelaide Microscopy in-house	monazite	450.2	3.4	10	451	2.69	20	453.8	4.7	
Ambat	Adelaide Microscopy in-house	monazite	520-525		10	517	2.8	20	519.4	3.99	
MG-1	Fletcher et al., 2004, Chemical Geology	xenotime	490	0.3	10	487.2	5.3	-	-	-	
Plesovice	Slama et al., 2008, Chem. Geol. 249, 1-35	zircon	337.13	0.37	20	337.9	2.2	-	-	-	
91500	Wiedenbeck et al. 95, Geostandards Newsletter 19, 1-23	zircon	1062.4	0.4	20	1061.8	6	-	-	-	

## 4. RESULTS

### 4.1 Petrology (Axioscan & M4 Tornado Micro Xrf)

Analysis of the granite samples from Figure 4 (1.6m, 300m, 600m & 700m) are seen as annotated photomicrographs in Figures 6 and 7, these act to summarise the broader trends observed geochemically across the granite from this study, discussed in the geochemistry portion of the results.

All samples are similar in basic characteristics of predominant minerals as quartz, K-feldspar, biotite, chlorite, and sericite. The start of drill hole CAR2038 (samples at 1.6m and 300m depth), is geochemically similar as in Figure 4. For this area, large >2mm phenocrysts of K-feldspar and quartz are dominant, with K-feldspar more elevated than quartz (AMICS data). Veining in this area is seen as (commonly) <2mm sized calcite and sericite veins, with length >50mm.

The 600m sample is geochemically similar to the 1.6m and 300m samples, however the mineralogy changes considerably. In this sample sericite is abundant, quartz is more abundant than K-feldspar. Sericite and calcite veins have increased in volume in the 600m sample relative to the 1.6m and 300m samples.

The 700m sample is far more depleted in K and enriched in Fe as seen in Figure 4, this sample is seen with Fe-rich K-feldspar, which sit amongst veins containing hematite and sericite. The 700m sample notably has decreased biotite and chlorite, and greatly increased in hematite relative to the 1.6m sample.

As seen in Figure 5, the 1.6m granite sample exhibits K-feldspar phenocrysts which have a small reaction rim of sericite where it is in contact with chlorite. When considering K-feldspars at 700m, Figure 6, much more sericite is seen rimming the



phenocrysts, with decreased chlorite. Sericite has replaced K-feldspar internally along apparent fracture planes in both samples, see Figure 7 in the SEM section of results, where Na-bearing feldspar is included in the K-feldspars in a similar pattern to that seen now replaced by sericite.

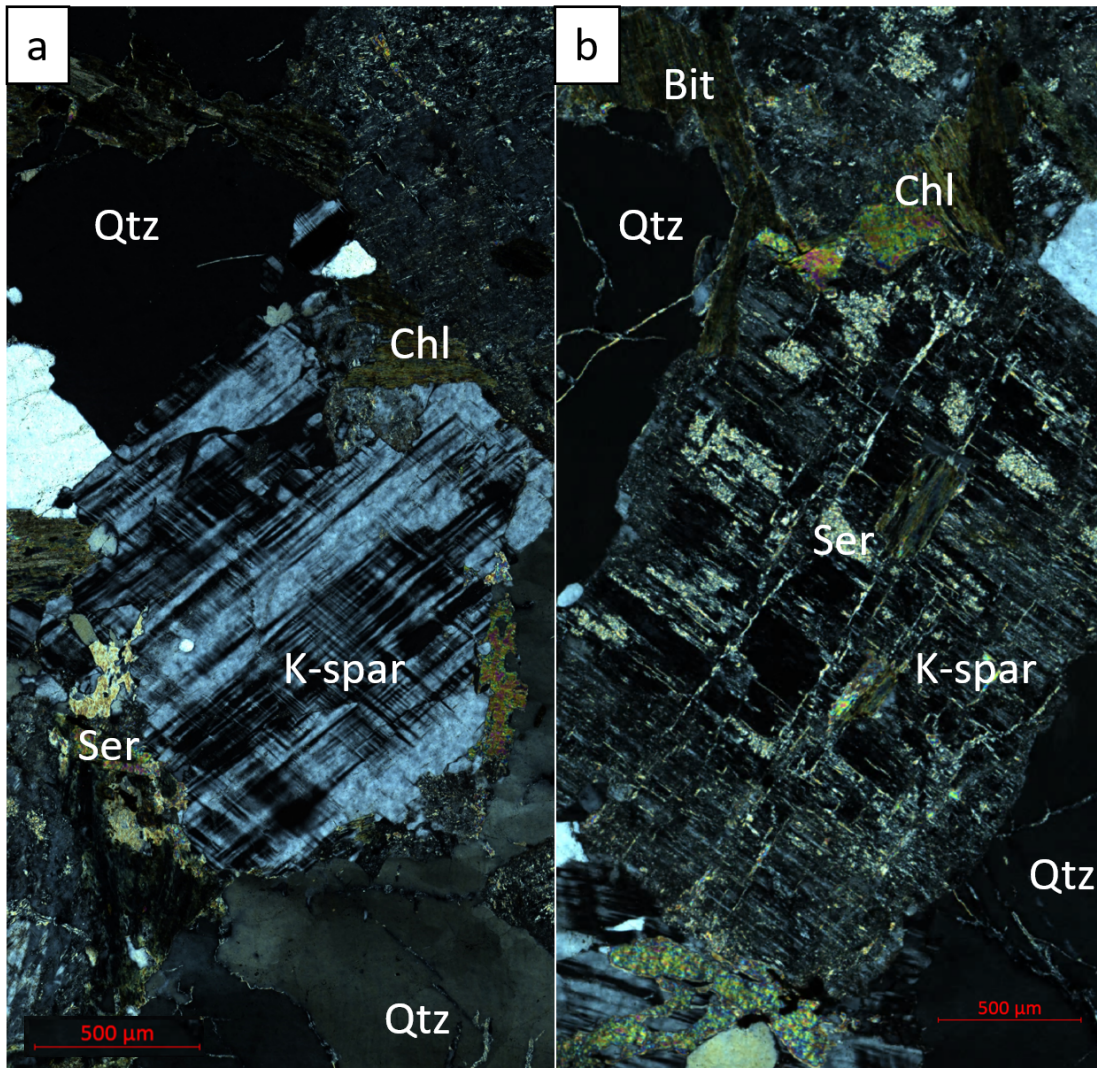


**Figure 5.** Axioscan XPL photomicrographs of 1.6m depth sample thin section from CAR2038. (a and b) K feldspar crystal, rimmed by sericite, with biotite and chlorite together wrapping larger quartz phenocrysts and sericite rims. (b) also shows an orthogonal veining texture where sericite has infilled space within the K-feldspar crystal. Qtz- quartz, Chl- chlorite, K-spar- K-feldspar, Bit- biotite, Ser- sericite.



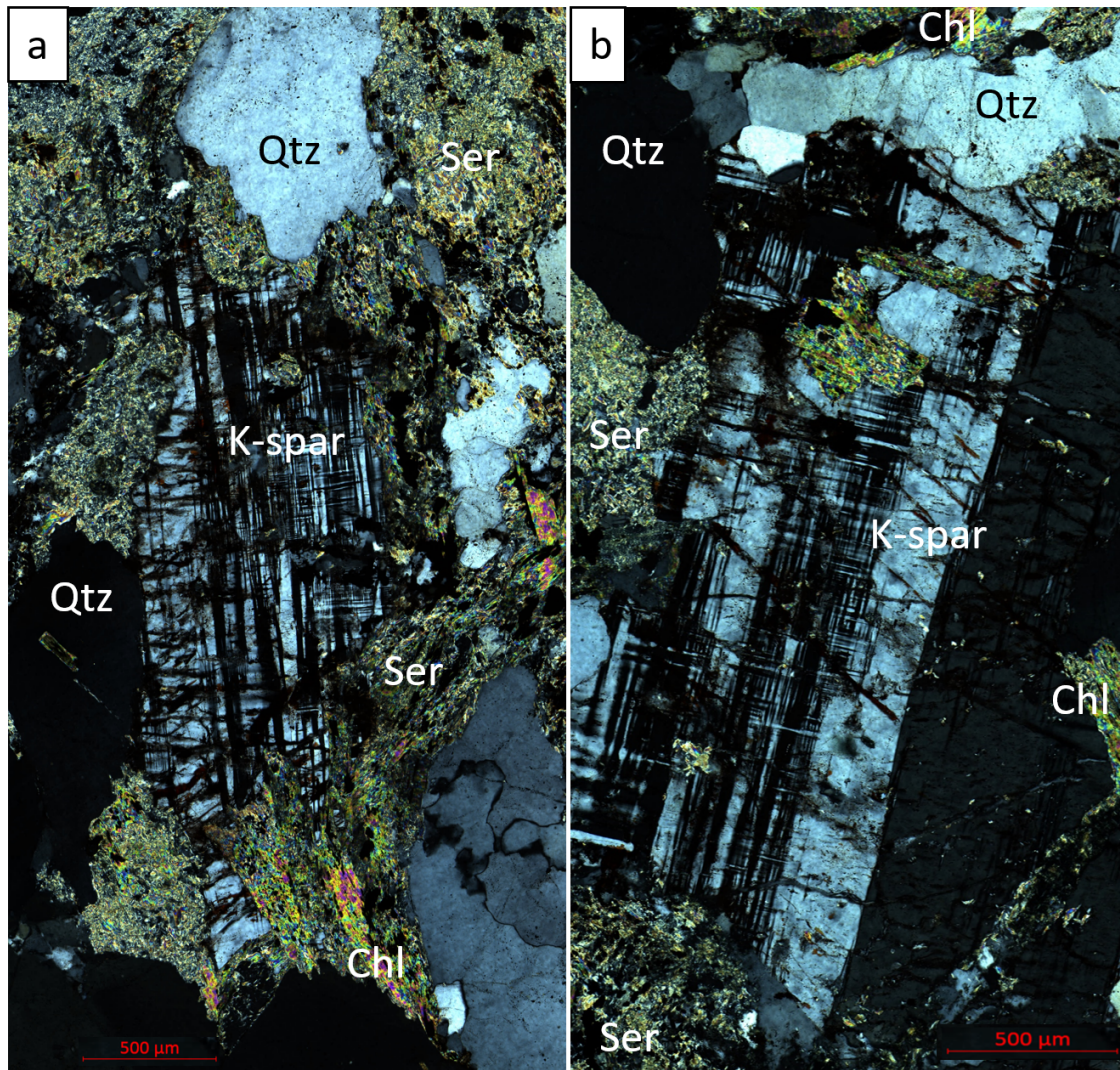


Figure 6. Axioscan XPL photomicrographs of 700m depth sample thin section from CAR2038. (a and b) show quartz is unaltered and does not have any reaction rimming. (a) K-feldspar, rimmed by sericite, phenocrysts of feldspar now sit in a fabric of sericite. (b) fractured potassium feldspar, chlorite is seen infilling and altering the crystal. Qtz- quartz, Chl- chlorite, K-spar- K-feldspar, Ser- sericite.

## 4.2 Scanning Electron Microscope and AMICS

The granite host rock around the deposit has undergone the following stages of alteration; First is wide scale chloritization reported broadly across the Donington Suite which is found in all granite samples (Courtney Davies et al 2019).

Later stages of alteration, which could be attributed to the Carrapateena ore system, are seen overprinting the chlorite with sericite and hematite. The strength of this relationship is a function of the minerals proximity to the CBC.

Na decreases towards the deposit relative to the average of further surrounding Donington Suite granite at 1km, 1.8km and 5.8km distance. Na bearing minerals, ie albite/plagioclase, observable in BSE are only seen in the first analysed granite sample at 1.6m distance in CAR2038. BSE images show albite overprinting k-feldspar to be a cross-hatched texture, in Figure 7. This sample is the only one exhibiting albite alteration seen for granite in this study.

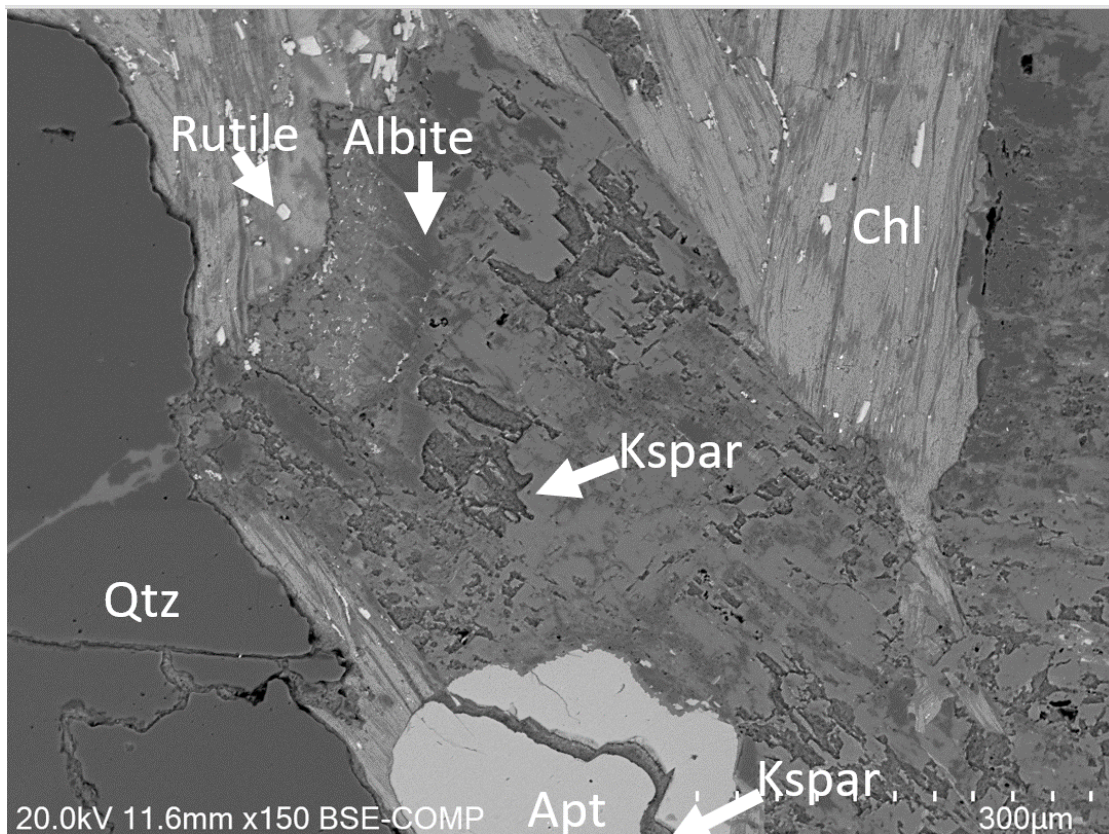


**Figure 7.** Back Scattered Electron image (Hitachi 3800) of 1.6m Sample CAR2038, apatite included in K-spar and in chlorite. Na-rich feldspar, albite, seen overprinting K-feldspar. Qtz- quartz, Chl- chlorite, K-spar- K-feldspar, Apt- apatite.



With depth, the persisting minerals are the most resilient/least reactive. Biotite and chlorite decrease towards the deposit, as these minerals are less resilient to hydrothermal alteration than the quartz and K-feldspars surrounding them. Sericite abundance increases toward the deposit, until the breccia zone of the CBC is intersected, ~725m depth in CAR2038, and sericite abundance decreases sharply related to geochemistry (Figure 4).

Apatite in CAR2038 has two characteristic textures, euhedral (Figure 8, d-i) and infilling anhedral shaped. Within the first 700m of CAR2038 the apatite is euhedral, while in the CBC, the apatite appears to be predominantly infilling. The later texture is potentially a precipitation texture, only a few apatite are seen as euhedral crystals when preserved by a resilient mineral on all sides, seen typically as inclusions in K-feldspar or quartz. Apatite is predominantly found on quartz and K-feldspar boundaries and is rarely seen included in these minerals, without the presence of fracture planes.

Similar to apatite, monazite occurs in two distinct shapes in CAR2038, a euhedral (Figure 8 j-o) and again as an infilling texture (Figure 9 c-h). Differing from the apatite, the anhedral (CBC) monazite is seen commonly with xenotime and including some sulphides, especially common in the ore zone. The inclusions and textures of monazite from within the deposit suggest they would preserve a mineralisation timing more than the apatite. AMICS images for granite and ore-zone samples act to summarise the mineral abundance as seen in Figure 8c where chlorite and albite are still abundant, which are removed in Figure 9b. More of the reflected in transition of minerals in granite-CBC are displayed through AMICS images from 300m, 600m and 700m (Appendix F).

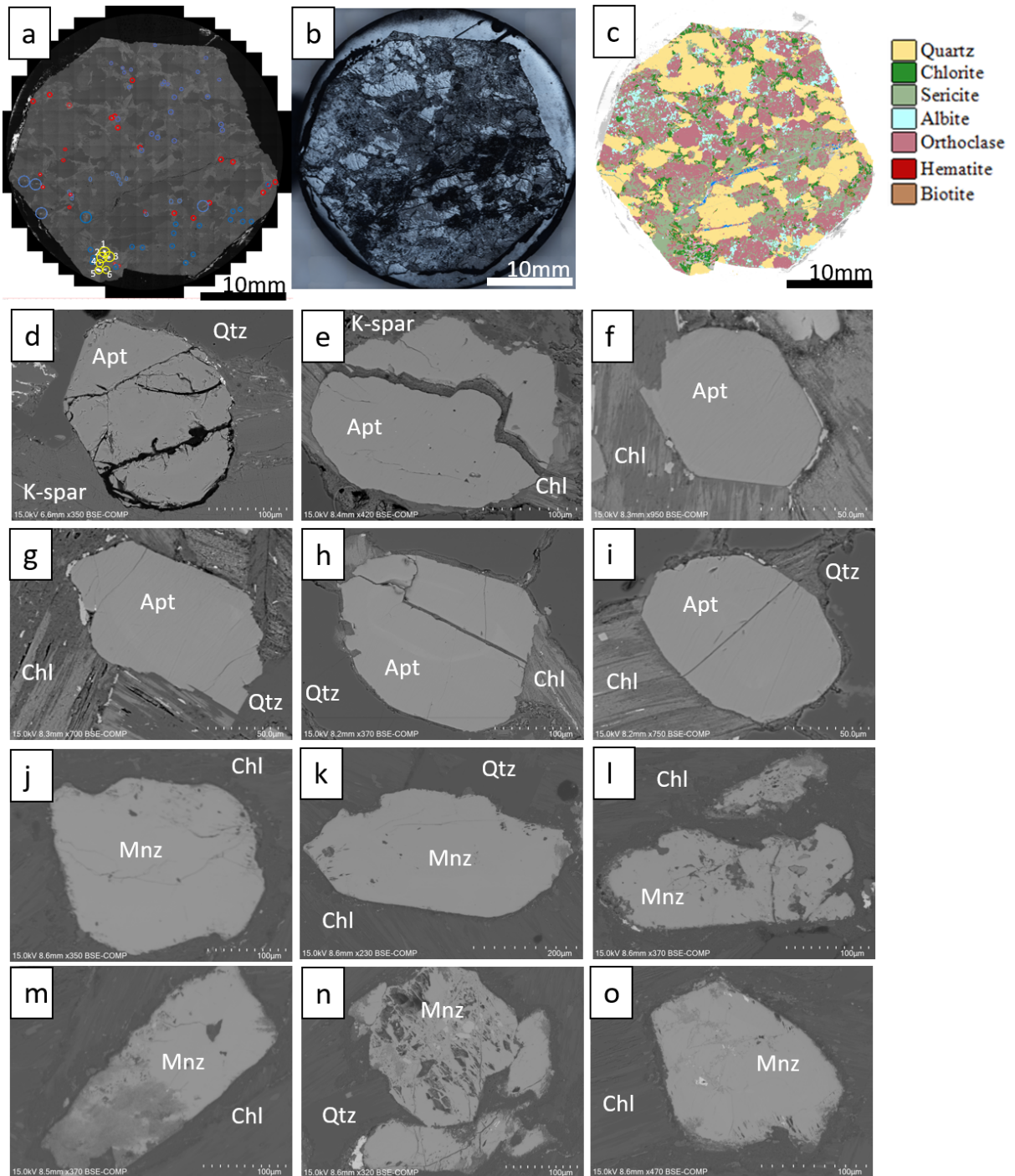


**Figure 8. Hitachi SEM 3800 granite 1" rock mount work, (a) Back Scatter Electron (BSE) image of CAR2038 drill hole granite sample from 1.6m depth, circled are target U-Pb dating minerals: red-zircon, blue-apatite, yellow-monazite. (b) Reflected light image from Adelaide Microscopy, showing topography of the polished sample. (c) AMICS (mineral charactering software) displaying mineral phase abundances. (d-i) Typical and characteristic shapes of apatite found in this sample. (j-o) Typical and characteristic size and shape of monazite in this sample. Qtz- quartz, Chl- chlorite, K-spar- K-feldspar, Apt- apatite, Mnz- monazite.**

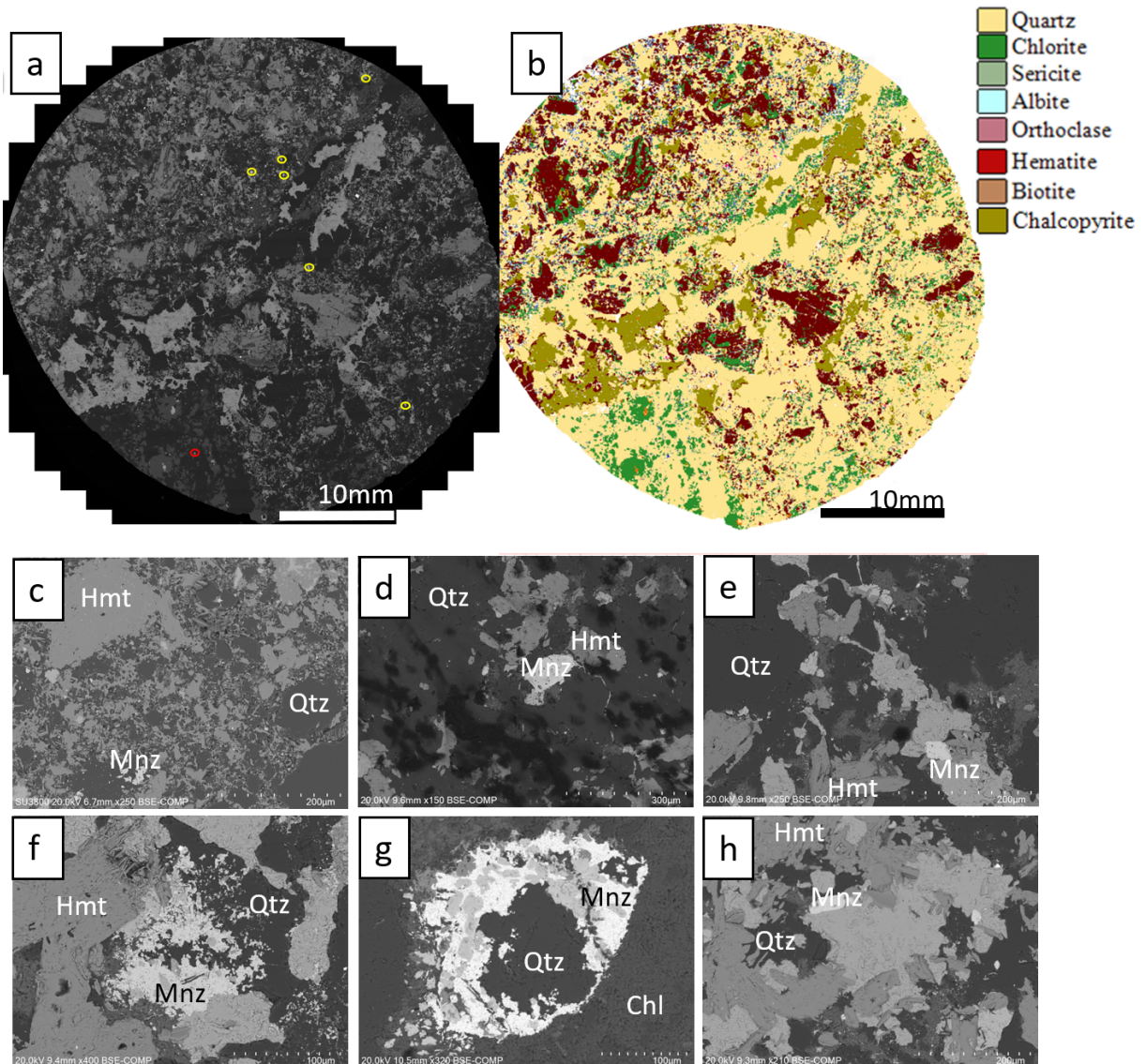


**Figure 9.** Hitachi SEM 3800 ore-zone/CBC 1” rock mount work, (a) Back Scatter Electron (BSE) image of CAR2038 drill hole ore-breccia sample from 1099m depth circled are target U-Pb dating minerals: red-zircon, yellow-monazite. (b) AMICS (mineral charactering software) displaying mineral phase abundances (Appendix F). (c-h) BSE images of typical monazite textures within the ore zone. Qtz- quartz, Chl- chlorite, K-spar- K-feldspar, Mnz- monazite, Hmt- hematite.

The AMICS map image generated for sample 1099m (Figure 9) shows the mineral phases which have resisted being altered or displaced away when inside the deposit.

Remaining minerals in this sample are quartz (yellow) chlorite and sericite (green).

Notably, biotite and albite are removed relative to Figure 8c AMICS image.

### 4.3 Micro XRF mapper

The petrographic observations are reiterated through the Tornado micro XRF images (Appendix D). The minerals in the granite (quartz, K-feldspars and micas) are subtly affected through the dispersion of elements such as Si, Al, K, Fe and Na, across the sample surface. Figure 10 shows the listed elements, with a base colour background (black) of Si. Figure 10a shows a dominant yellow and grey assemblage (feldspars and quartz). Green colouring shows the feldspars which are all at least moderately K rich ranging to highly K rich. Linear features running across the image are correlated to veins. Blue colouration shows that some Na is preserved in this sample, though it is only found in any large extent as inclusions in quartz, suggesting the feldspars are not able to retain Na in the system. Red colouration for Fe content shows the majority of Fe at this part of the drillhole is concentrated in the chlorite which surrounds the feldspars. Figure 10b shows the more ore-body proximal sample at 700m depth in the same colouration as Figure 10a. The major differences can be seen as more grey colouration - as quartz is enriched. K from the feldspars is now decreased and more evenly distributed through the sample. Very little to no Na is left, at 700m depth of the drillhole. Fe can be seen intruding into feldspars and is now seen veining through the sample in the form of hematite, but not as an incorporated element in micas as seen in Figure 10a.



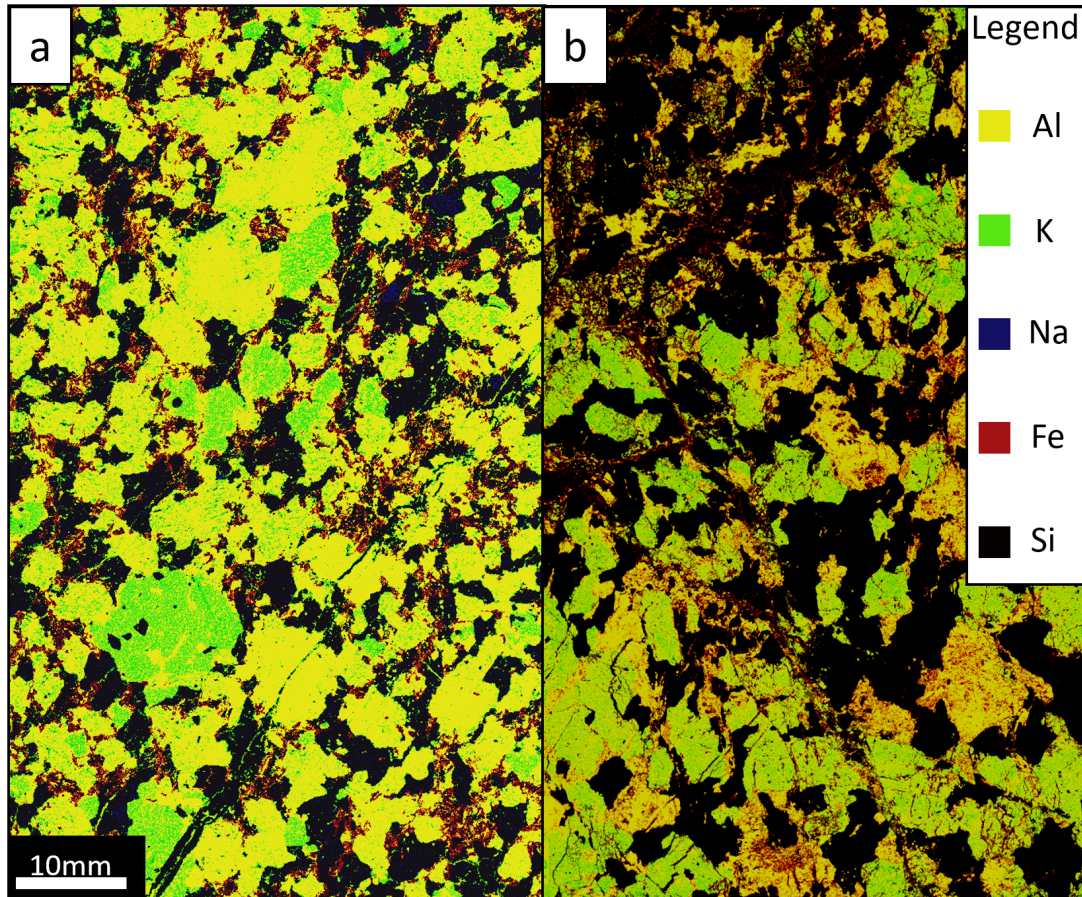


Figure 10. Micro XRF images taken on m4 Tornado machine Adelaide Microscopy of CAR2038, (a) from 1.6m sample. (b) from 700m sample. Displaying Silicon (black) aluminium (yellow), Iron (red), Sodium (blue) and potassium (green). Minerals which contain multiple elements listed here can be distinguished by colour of their dominant element. Yellow (Al) depicts all feldspar present, while green (K) depict K-feldspar. Red (Fe) is predominantly in chlorite in (a), and in hematite in (b), veining and replacing across the feldspars and sericite. (a) interpreted as ~25% quartz (black), with >50 Ca-Na feldspar (yellow) with areas of very K-rich (green), chlorite (red) wrapping feldspar. (b) interpreted as ~50% quartz, Ca-Na feldspars less dominant than K-feldspar, and hematite (red) veining through feldspars.

#### 4.4 Whole Rock Geochemistry

Geochemical data for the first 700m of drillhole CAR2038 core is presented in Figure 4, where a basic summary of major elements, copper enrichment and Y (Heavy REE proxy) summarises the granites major geochemical variation. Figure 11a continues Figure 4 and shows the highest concentration elements for the drill hole, which presents the increase of Fe towards the deposit and the related decrease of other majors like Al,



K and most affected is Si. The Si/Fe inflection point at ~725m depth is the transition from granitic composition to hematite ore breccia.

Figure 11a shows K for CAR2038, which is incorporated in the structure of sericite, and decreases from over 30,000ppm to under 5000ppm at the CBC boundary (~725m depth). The sericite and K-feldspar decrease are related to the increase of hematite and the removal of other mineral phases, seen through the major element geochemistry in Figure 11a. The most significant variation is seen at ~730m where Si content is greatly replaced by Fe, attributed to the CBC and hematite ore. Another major element change seen at ~670m where Fe content becomes elevated over the Al and K.

Figure 11b shows the mentioned transition from granite to ore breccia is more gradual for Cu. The gradual transition in the other chalcophile elements is less pronounced, where the sudden detection of Se and Ni is recorded at or near the inflection point.

Trace elements in the drillhole again show trends which are more gradual than the major element transition, except for F, which decreases sharply at the ~725m inflection point noted in the major element plot (Figure 11 c). Au and Ce increase from before 700m depth, where the inflection point is recorded a further ~30m down drillhole. Na content is elevated at the start of the drillhole and Y(REE proxy) content becomes more variable approaching the CBC.

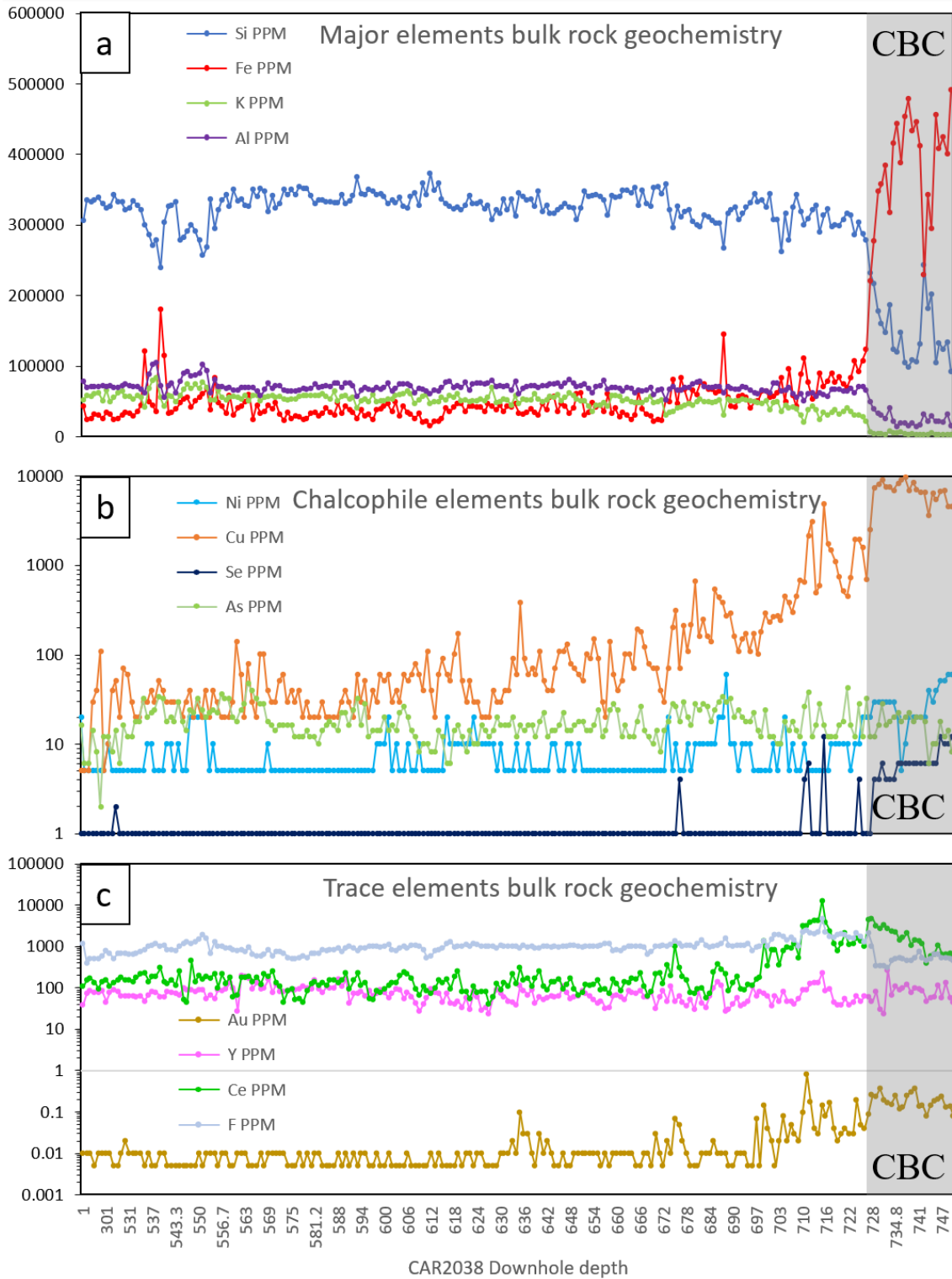


**Figure 11. Geochemical plots from CAR2038 bulk rock assay data. (a) major element compositions of >8% (b), chalcophile elements with detectable variation. (c) trace elements with interest of this report, where Y is used as proxy for REEs. Grey zone from ~725m where the CBC is interpreted to begin.**

A comparison of alkali metal concentration in Figure 12 shows that Na/K is diminished close to the deposit, relative to the regional (<5.8km) granite. Na decreases from an average 7000ppm over the first 400m of drillhole, down to 2000ppm over the remaining drillhole. This is compared to K which decreases suddenly at the transition from granite to ore breccia, from 55,000ppm to <10,000ppm.

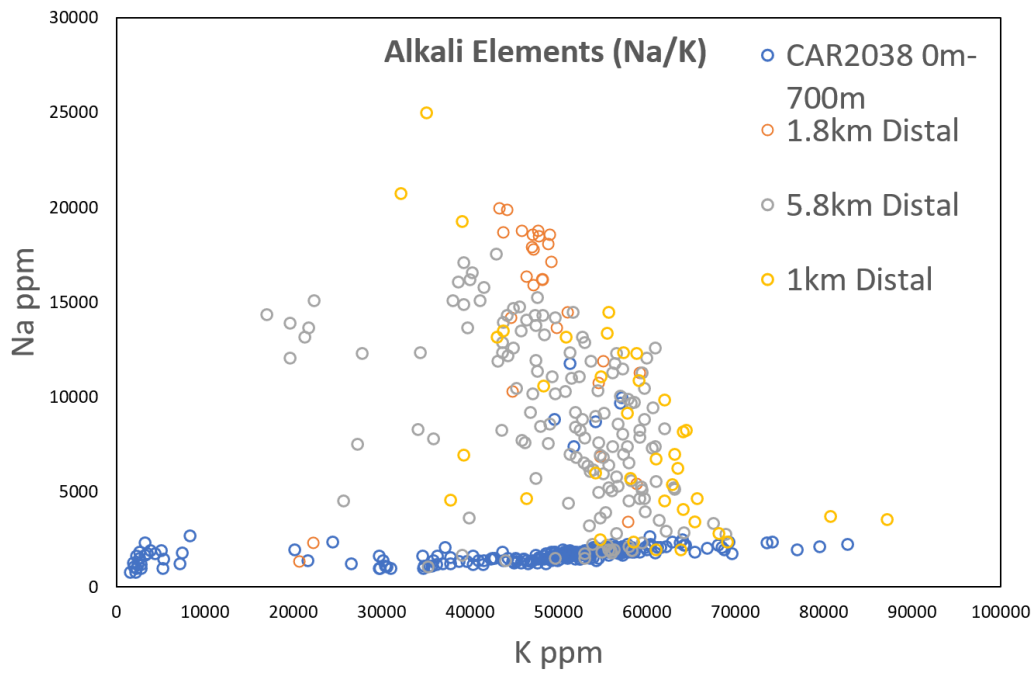


**Figure 12. Alkali element concentration (Na/K) of CAR2038 and distal drillholes- DD12GIL001 (5.8km) DD12CAR116W1 (1.8km) and DD13CAR117W1 (1km). CAR2038 (hollow blue points), Trend follows a path immediately down (Sole loss of Na) and then across to the left (sole loss of K), Na decreasing first for the initial 1m- 300m of drillhole, followed by K decreasing from 400m to 750m of drillhole this demonstrates the two elements decrease independently.**

#### **4.5 U-PB GEOCHRONOLOGY**

In order to analyse the age of mineral phases, geochronology has been completed on minerals which are associated to hydrothermal activity and to the magmatic system which produced the host rock.

Geochronology was undertaken in conjunction with trace/REE using the LA-ICP MS. Selection of mineral targets was complete with the BSE images generated (Appendix A), in accompaniment with AMICS mineral maps (Appendix F), on the Hitachi 3800. These produced targets of sizes; zircon 30-90 micron, monazite 50-200micron, xenotime 20-150micron and apatite 50-200 micron, examples available (Appendix C). Plotting of Concordia diagrams was based on Iolite data-reduction in conjunction with trace element analysis. Yttrium, zirconium, cerium, calcium and phosphorus values outside the selection criteria (Appendix G) were omitted in an effort to refine the quality of mineral data. Secondary standards as reported in Table 3 for verification steps. Target minerals in the Ore-zone samples have very large errors in the data and do not provide reliable statistical ages. Due to the limited background data on dating events in the deposit, ages will still be presented to exhibit the limitations of geochronology in the ore system, and to demonstrate how the minerals are affected comparatively with granite samples, however the data is considered to be a range of concordant ages, rather than a statistical age.

##### **4.5.1 Apatite Geochronology, REE Chemistry**

Figure 13 shows the isochron age for apatite from the granite and CBC for CAR2038. Samples within the granite Figure 13 (a & b)- (1.6m and 600m) have strong correlation for the common Pb trend presented in the plots, and therefore produce a more precise age. Apatite at 1.6m depth in the drillhole are  $1765 \pm 18$  Ma, and at 600m depth are

1781 ± 23Ma. Apatite from inside the orebody do not record precise age ranges and are presented to show the variability in sample errors and the correlation between them.

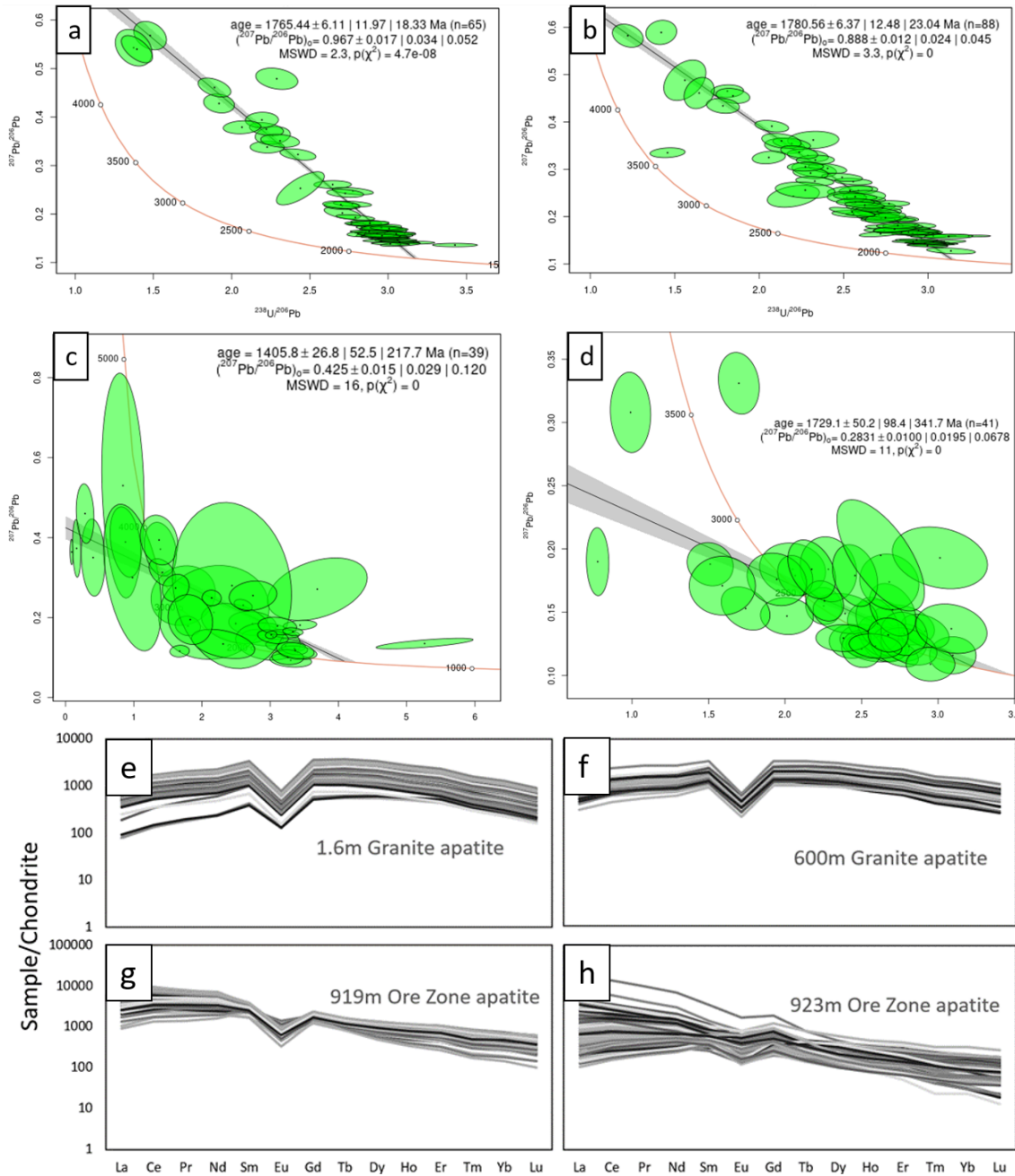


**Figure 13.** Apatite Terra-wasserburg plots, concordant secondary standards report in (Appendix E). All samples from CAR2038 drillhole. Age reported is the isochron (black line) intercept (lower) with the concordia curve, which is the age of closure temperature for each sample set. The MSWD is the Mean Square of Weighted Deviates for concordance. (a and b) Apatite from granite samples, euohedral and providing an age of 1765Ma & 1780Ma respectively. (c and d) Apatite from orebody, very anhedral forming infill textures, highly dispersed data with no statistical age producible as evident from MSWD. (e-h) REE concentrations from trace element data for apatite. (e) 1.6m and, (f) 600m, taken from granite samples. (g and h) taken from Bornite Zone samples 919m and 923m. (all units in PPM as exported from Iolite DRS).

Apatite REE signatures across the CAR2038 drillhole exhibit relative enrichment of the LREEs, with a consistent depletion in Eu (Figure 13 e-h). Ore zone apatite display a more significant depletion in HREEs, with some slight enrichment in LREEs also. The granite samples from more euhedral apatite provide more consistent and uniform analysis, while ore zone REEs are more variable.

#### **4.5.2 Monazite Geochronology & REE Chemistry**

Figure 14 Shows the geochronology obtained from LA-ICP-MS on monazite in CAR2038. Monazite found in the granite (1.6m sample Figure 14 b), considering concordant data only, has a weighted mean Pb207/206 age of  $1835.8 \pm 4.2$  Ma, which is similar to a Donington Suite aged granite (~1850Ma, Mortimer et al., 1988).

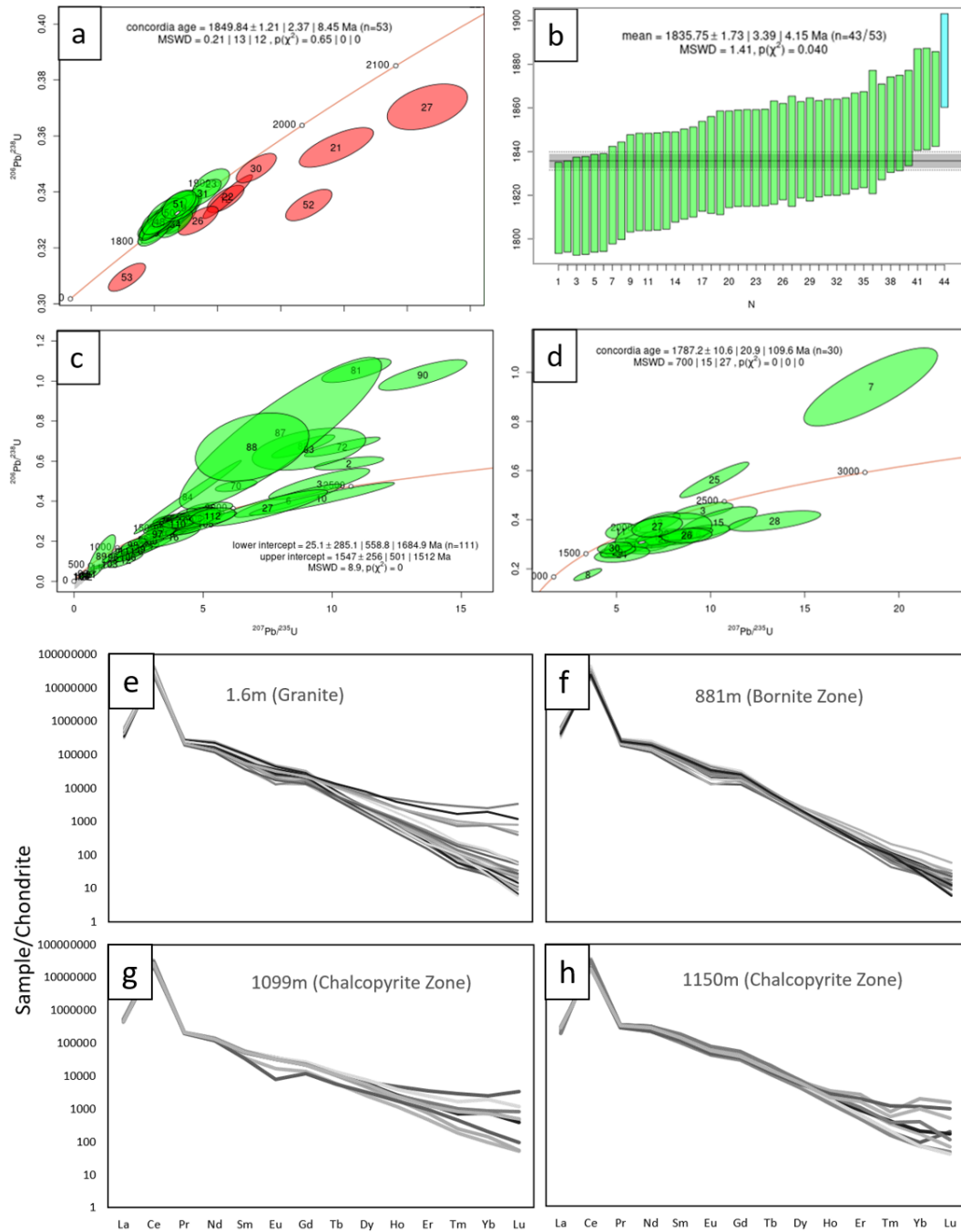


**Figure 14.** (a) and (b) 1.6m CAR2038 granite, (a) monazite Wetherill green ellipses concordant data only, red ellipses are discordant (b) weighted mean age only considering concordant data. (c) and (d) both have highly dispersed data and through the MSWD do not produce statistical ages. (c) 1099m depth (Chalcopyrite Zone) sample, discordant and reversely discordant data as sample monazites were full of inclusions. (d) 881m (Bornite Zone) sample, discordant monazite both common Pb and modern Pb loss affected. Modern lead loss affects described in all samples as ages are pulled down and left to younger ages. Common lead affects are seen in all samples as ages are pulled up and right to resemble older ages, Pb affects expanded in discussion. (e-h) Trace element data from ICP-MS, monazite REE, show similar trends for monazites across CAR2038, grey-shading of each line to differentiate minerals within each sample. (e) sample from 1.6m depth showing typical granite monazite trace element chemistry. (f) showing ore deposit Bornite Zone (881m) monazite chemistry. (g and h) showing Chalcopyrite Zone 1099 and 1150m depths monazite. (All units in PPM as exported from Iolite DRS)

Monazites from the Bornite Zone are more significantly affected by inclusions and appear to have more convoluted geochronology results (Figure 14 c & d). These Wetherill-plots show the monazite has included common Pb at formation which brought their ages to be older, while also experiencing a trend of modern Pb loss which has brought ages down younger to varying degrees across the samples. The intersection and concordant data suggest (imprecisely) the monazites within the Bornite Zone (881m) record the age similar to that of the apatite. While the Chalcopyrite Zone (1099m) monazite suggests (very imprecisely), the monazite grew approximately associated to the ore forming Hiltaba Suite magmatism timing.

REE plots generated from trace element data seen in Figure 14, show how the monazite composition changes through the drillhole. The monazite from the host granite sample (1.6m) retains the distinct negative Eu anomaly which has been seen in apatite, while each of the ore zone sample monazites have less pronounced negative Eu anomalies. The spread/variability in the granite sample is much tighter than the ore zone samples which also have a strong depletion progressing through the HREEs.

#### **4.5.3 Xenotime geochronology & REE chemistry**

Xenotime in the CAR2038 samples is rare and only found in sufficient size for analysis in the 700m granite sample as well as some inclusions of xenotime in monazite from around the ore zone, as a mottled texture with fine inclusions of other REE bearing minerals. The 700m sample as seen in Figure 15, has been affected by some common Pb, through the inclusions seen in (Appendix C), potentially increasing the reported age of some analyses and creating discordia. The sample also sees modern Pb loss affects which have depleted the samples Pb content and subsequently brought the samples ages down younger and hence has required an intercept age rather than concordant data. The



xenotime data from 600m xenotime (Figure 15 a) loosely describes a Donington Suite age at  $1882.6 \pm 65$ Ma, while the xenotime at 700m (Figure 15 b) describes a more accurate (less precise) Donington Suite age at  $1844.87 \pm 78.8$  Ma.

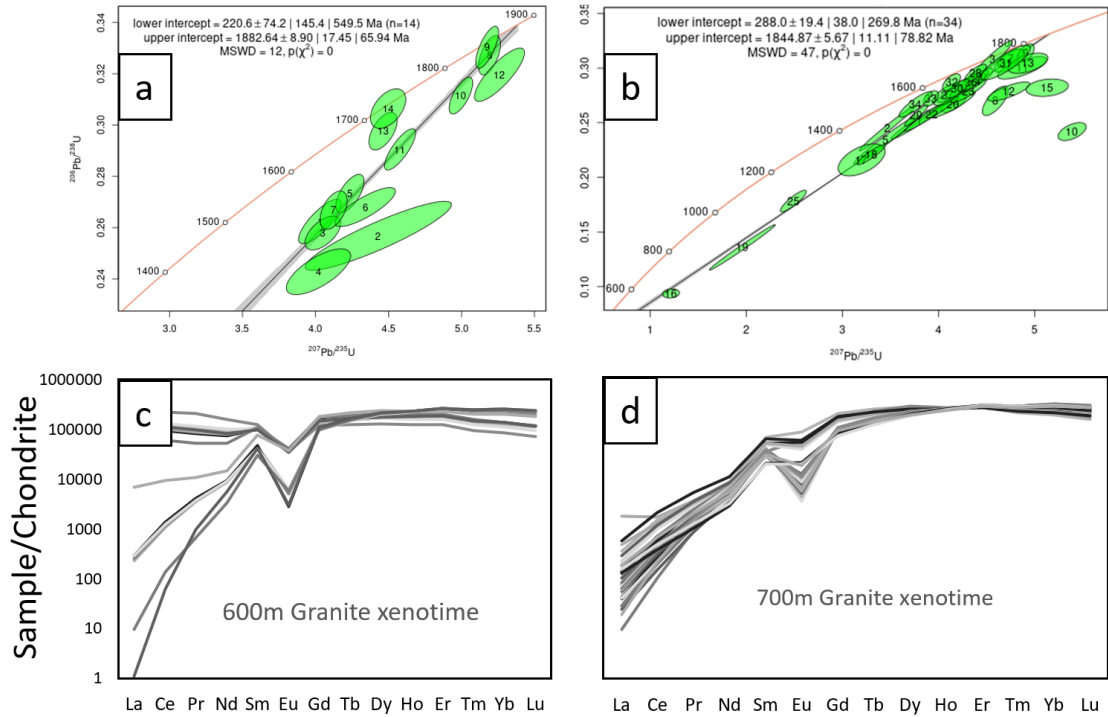


**Figure 15. (a) and (b), Isochron age for xenotime from CAR2038, 600m and 700m samples displaying ages of ~1883 and ~1844 Ma respectively, IsoplotR. (c) and (d) Xenotime REE concentrations from LA-ICP MS data. 600m (c) Granite sample consisting of fine anhedral xenotime as seen in (Appendix C), 700m (d) granite sample of large grained xenotime, with inclusions as seen in (Appendix C). (all units in PPM as exported from Iolite DRS).**

Xenotime in CAR2038 was analysed with REEs as seen in Figure 15(c & d). These plots show the variation in the 600m sample, which still retains a small negative Eu anomaly which has been noted in other REE bearing minerals. The spread in LREEs could be due to small inclusions which were present in the very fine xenotime. The 700m sample had significantly larger crystals though still hosting inclusions, this sample is seen with a strong depletion in LREEs and continuing to show the negative Eu anomaly.

#### **4.5.4 Zircon Geochronology & REE chemistry**

The zircons recorded in CAR2038 were found to be euhedral and of sizes averaging at 30 microns. The zircons were zoned with multiple generations in some crystals, with typically two zones preserved in most crystals. Due to the size of zircons, high precision on zonation in conjunction with the ages recorded couldn't be retained, however based on the isochrons seen below, it seems only one generation/time is recorded, when considering modern Pb loss. The isochrons in Figure 16 a & b show the spread in modern Pb loss affected zircons which plot linearly down to the lower intercept age of approximately the modern day. Zircons from the 1.6m sample (Figure 16a) record an age similar to that recorded by apatite in the granite. Zircon from the 600m sample retains an older age more similar to monazite from 1.6m depth (CAR2038) in the granite.

The related geochemistry of these samples is seen in Figure 16 (c & d), showing both sets are affected by the Eu depletion trend seen throughout the tested minerals so far, and significant increase in Ce for the 1.6m zircons.

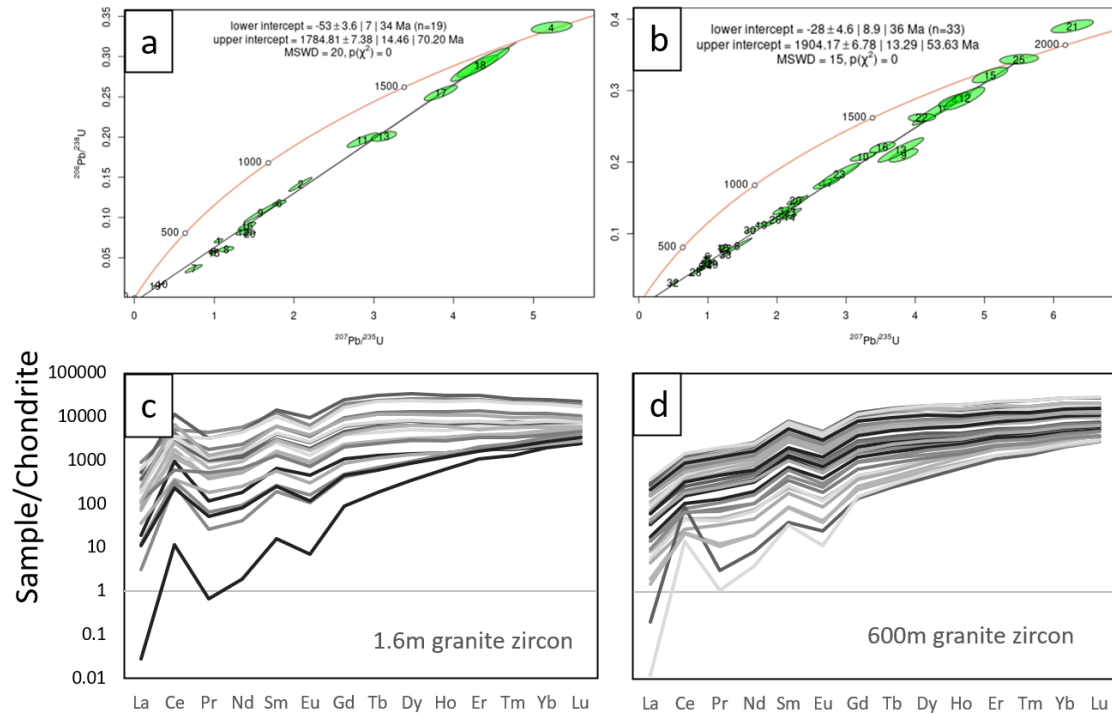


**Figure 16.** Zircons from CAR2038 Drill hole with closure temperature isochron age as upper intercept. (a) 1.6m sample,  $1784 \pm 70 \text{ Ma}$ . (b), 600m sample,  $1904 \pm 54 \text{ Ma}$ . (c) and (d) Trace element data from LA-ICP MS session, building the REE plot. (c) 1.6m granite sample, consistent HREEs, and enriched Ce with depleted LREE. (d) 600m granite sample with depleted LREE and negative Eu anomaly, enriched in HREE and more uniform analyses.

## 5 DISCUSSION

The hydrothermal alteration of the Carrapateena deposit and surrounding granite is aimed to be investigated through mineralogy, geochronology, and geochemical methods in this study. By combining the observed features found in these areas, the nature of the Carrapateena deposit alteration halo and hydrothermal event history can be better understood.

### 5.1 Mineralogical relationships and textures described in petrology

Petrographic analysis with BSE and optical microscope work shows the main alteration features change as a function of distance from the deposit. Biotite is common in both granodiorites and granites, both of which, the local Donington Suite has the appropriate composition (Appendix J). Alteration of Donington Suite biotite to form chlorite (Brotodewo 2020) is seen at the widest scale, (Figure 5), as the host granite could have had a more biotite rich starting composition which has reacted with hydrothermal fluids. The chlorite alteration of Donington Suite biotite requires water (Eggleton and Banfield 1985), which have could been liberated from the of exhuming material, such as the Wallaroo Group timing extensional magmatism and Hiltaba Suite, of which the apatite data (Figure 13 a and b) suggests chlorite apatite is older than the Hiltaba Suite. Biotite and alteration to form chlorite are not seen in the 700m depth granite (Appendix F), likely as these minerals are more reactive with hydrothermal fluids which are leaving the CBC, with only minor chlorite left in granite rafts supported by the hematite breccia. Sericite alteration in CAR2038 increases towards the deposit, replacing chlorite when in contact with K-feldspar, and in areas where plagioclase was interpreted to have been. This is potentially as the surrounding feldspars were more chemically susceptible to acidic IOCG hydrothermal fluids (Tappert et al, 2013), where plagioclase was replaced

initially (Kontonikas-Charos et al 2016) and K-feldspar begins to reject the most volatile element in their crystal structure K, which was accommodated by the surrounding micas, to form sericite. This subsequently would have replaced Fe and Mg in the chlorite, enriching either the hematite veins surrounding the sericite or adding Fe to the feldspar composition.

Feldspars in the host granite around the CBC have relationships seen in Figure 5, which show the 1.6m depth sample, with Na-rich feldspar (albite) included in K-feldspar. This texture is then seen in deeper samples, however the included shape left in the K-feldspar is infilled by chlorite and sericite. This suggests albite was in the granite system, either during the granites diagenesis (sodic plagioclase) or as albite alteration, and reacted to form sericite and chlorite, during or before the ore-stage fluids, which have been able to remove/replace albite with growth of sericite and chlorite.

## **5.2 Interpretation of U-Pb geochronology and trace elements**

U-Pb geochronology of xenotime, zircon and monazite from the granite in the CAR2038 drillhole has produced Donington Suite related ages with the exception of zircon at 1.6m (Figure 16a), these are compared to other deposits on the Stuart Shelf in Figure 17, where granite data (green) is seen with more precision than ore-zone data (red). The Donington Suite is dated to ~1850Ma, (Mortimer et al., 1988), while the mentioned minerals analysed in the CAR2038 drillhole granite report ages from 1844-1890Ma (Figures 15,16 &17).

When assessing the recorded isochron age for apatite in granite samples, the ~1780Ma timing preserved does not coincide with the host- Donington Suite granite cooling age, nor does it align with the ore-forming fluid age range (~1598Ma Sawyer 2017).

The apatite from CAR2038 record ages of 1765-1780Ma (Figure 13 a & b), these align closely to the 1.6m zircon timing (Figure 16 a). This timing has potential to be generated by a series of options, with a few of the most likely being: Slow cooling from Donington Suite age, reheating and partial resetting of Donington Suite magmatic apatite, and finally hydrothermal growth of apatite correlated to McGregor Volcanics (1740Ma Fanning 1988) and Wallaroo Group timing (1765 to 1740Ma Hand et al 2007).

Both the reheating and slow cooling options would infer that apatite has not changed bulk composition since its growth in the Donington Suite, and have only experienced thermal events which have generated statistical ages younger than the apatite growth. Apatite compositions reflect the compositions of the system it formed in (Sha and Chappell 1999). Texturally CAR2038 apatites aren't included in the quartz and K-feldspar, and are only seen on the edges of these grains (Figure 7), which supports the apatite forming later, rather than slow cooling ore reheating, as apatite would be expected to have formed some minor inclusions in quartz crystals as the Donington Suite cooled.

The negative Eu anomaly in apatite (Figure 14) are inconsistent with peraluminous granites of both S and I-type (Sha and Chappell 1999). Apatite-Th content averaged 15.8ppm suggesting the apatite are sourced from S-type granites (<30ppm Sha and Chappell 1999), further suggesting the apatite didn't grow with the I-type Donington Suite (Curtis 2019).

The apatite timing is within error of the Wallaroo Group timing of ~1765 to 1740Ma (Hand et al 2007), however there isn't yet evidence for this group at Carrapateena.

Wallaroo Group is predominantly sedimentary sequence, associated with extension and

rifting which correlated to granitic rocks that intruded bedrock (Donington Suite granite) at 1.75Ga, and are recorded 30km North of Olympic Dam (Courtney-Davies 2020).

Work from Courtney-Davies et al 2020, has found a dominant age in Olympic Dam magnetite dating is  $\sim 1760 \pm 16$ Ma, which is older than Hiltaba magmatism (mineralisation) and older than Roxby Downs granite (RDG) 1593Ma. Courtney-Davies et al. found correlation with the meta-sedimentary Wallaroo Group, speculating this unit to have exsolved hydrothermal fluids. The ages of CAR2038 apatite and zircon seen in the granite suggest an event of similar timing occurred at Carrapateena. The significance of magnetite age found in this study is questionable, based on the drill hole's location in the near centre of Olympic Dam, with >5Km of surrounding RDG, suggesting the age calculated would be from a xenolith which is brought into the RDG, rather than a magmatic or hydrothermal event.

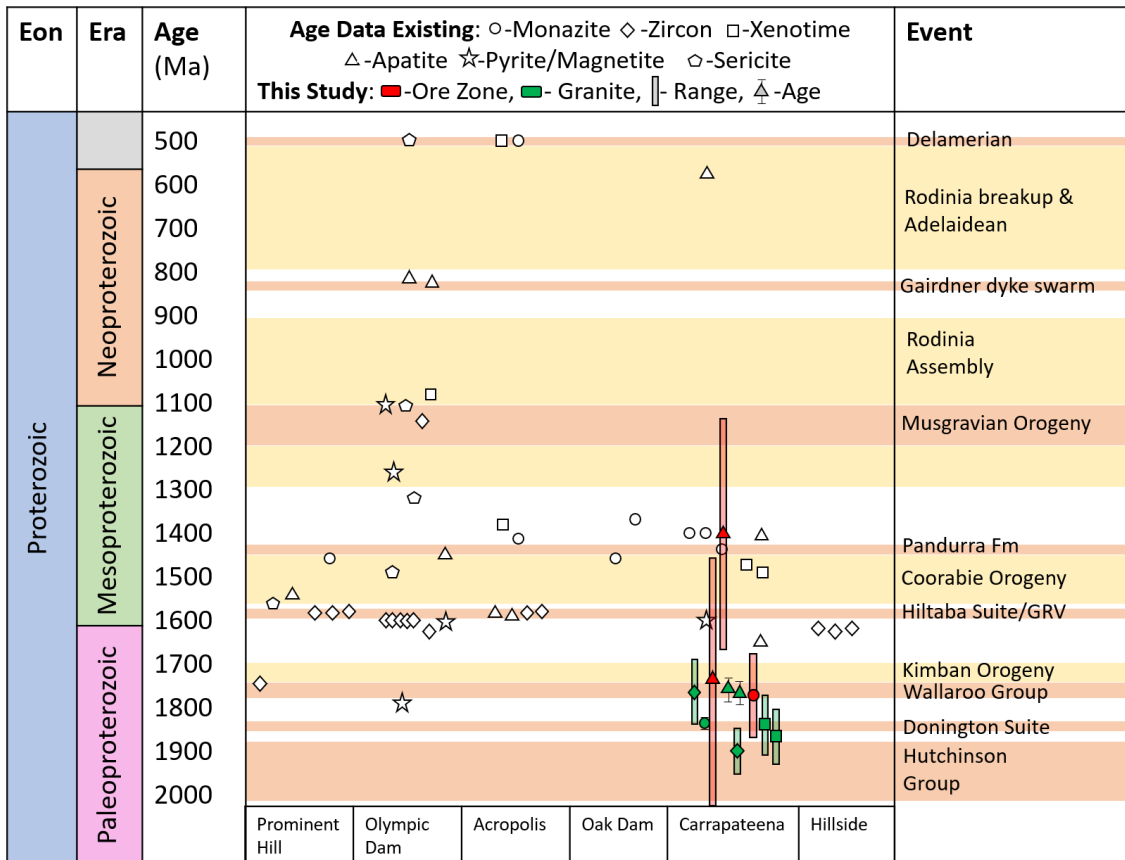


**Figure 17. Time Space plot for geochronology completed across IOCG deposits on the Stuart Shelf modified from B. North 2020. Minerals from this study are presenting either a statistical age with associated error margins, or a range of potential ages based on concordant geochronology data. IOCG deposits ordered North (Prominent Hill) to South (Hillside). Events preserved in the region are shown for reference on mineralisation ages. Age data for Prominent Hill Bowden et al. (2016), Belperio et al. (2007) and Jagodzinski et al. (2007). Age data for Olympic Dam Gustafson and Compston (1979), Maas et al. (2011), McInnes et al. (2008), Cherry et al. (2017), Cherry et al. (2018), Lane (2015), Apukhtina et al. (2017), Huang et al. (2015) and Mcphie et al. (2020). Age data for Acropolis Cherry et al. (2018) and Mcphie et al. (2020). Age data for Oak Dam (Oak Dam East) sourced from Davidson et al. (2007). Age data for Carrapateena Sawyer et al. (2017), North (2020) and this study. Age data for Hillside from Gregory et al. (2011).**

Zircon from the 1.6m sample and apatite from 1.6m, and 600m samples correlate to Wallaroo Group timing (Figure 17). Zircon from the 1.6m sample (younger age range) have a more variable composition, with higher enrichment of LREEs than zircon in the 600m sample (older age range) (Figure 16 c and d), which provides further evidence for these minerals being formed/reset at different times.

Geochronology suggests that the apatite in granite immediately surrounding the deposit was not thermally reset by Hiltaba (~1590Ma) aged events. This suggests granite-apatite



immediately surrounding the CBC during the emplacement of hematite-ore was either thermally unaffected/protected, or at least that partial thermal resetting of the apatite was not sustained long enough to completely reset them.

Hematite-bearing IOCG fluids are expected to be <400 °C (Reid et al 2019). If apatite, with a closure temperature of 375-600 °C (Kirkland et al 2018) ~ within 150m of the orebody (Figure 13 b), have not received enough heat to be thermally reset by the ore-forming events centred around Hiltaba (~1590 Ma) timing, then this could be evidence for a maximum heat production from the deposit during emplacement.

Monazite geochronology seen in Figure 14 shows the granite intersected at the start of the drillhole is of the expected age, synchronous with other Donington Suite granites described. The monazite become finer and more anhedral with depth and approaching the ore zone. These monazites retain their 'concordant' age. However, many analyses also retain discordant ages, which can be attributed to the common Pb, suggesting that excess Pb was already incorporated into the crystal when it formed. Zircon xenotime and apatite also preserve the effects of both common Pb and modern Pb loss. The resultant Concordia plots exhibit the common Pb affected analyses being brought down by 'modern Pb loss' resulting in strongly discordant data as demonstrated in Figure 18.

It is through inclusions and the common Pb, modern Pb loss trends, that the errors on Figure 17 become so large.

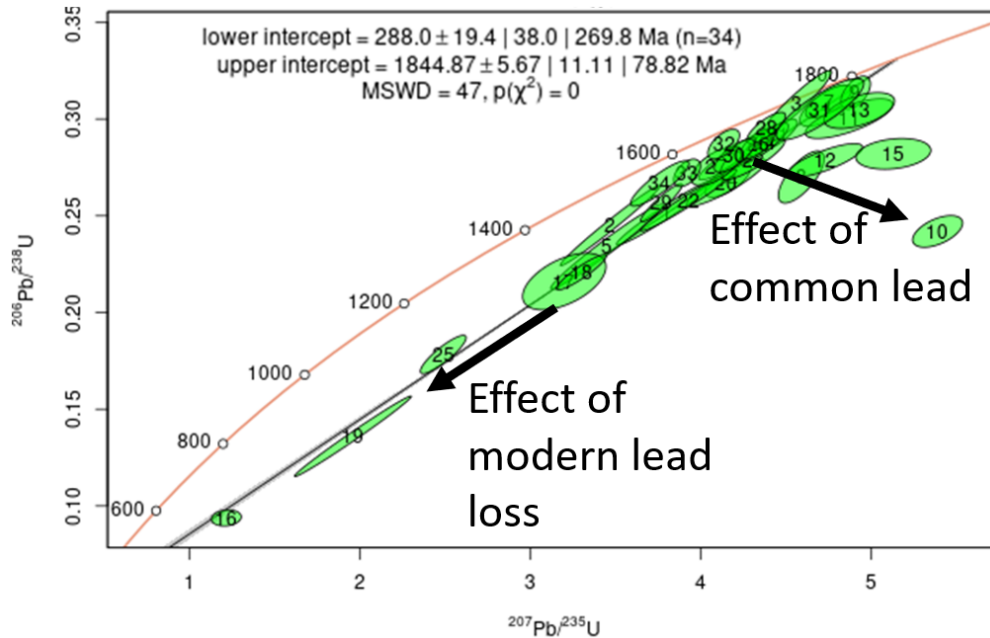


Figure 18. Xenotime from 700m sample CAR2038 plotted using iolite in Wetherill space, exhibits some concordant data, with (excess) common Pb in the system before the xenotime grew pulling ages further back in age (to the right). Modern Pb loss trend pulls ages into Discordia down to younger ages.

### 5.3 Interpretation of geochemical data

Albitic alteration is common in many IOCG deposits, however in this deposit, Na concentration and albite is only found 700m away from the ore zone. Na depletion is well expressed in the alkali element plot Na:K, Figure 12, where the relative enrichment of K can be seen stronger for the blue datapoints - CAR2038 drill hole bulk geochemistry, than the comparatively weaker enrichment more distal drillholes. This could suggest that the ore-forming fluids from the Carrapateena deposit were capable of stripping Na from minerals such as albite, but not significantly affecting the K-feldspars.

Figure 19 combines CAR2013 Na:K ratios, with the concentration of Fe and the distance from the deposit. Combining these allows for comparison similar to Olympic Dam's interpreted alteration stages (Ehrig 2013). Through this chart the 'extent' of sericite to K-feldspar extends for 350m (750m-400m downhole depth CAR2038), while the Plagioclase to sericite extent is retained for a further 400m (400m-1.6m depth in CAR2038), Limited to the single drill hole tested and to the 50m tested intervals.

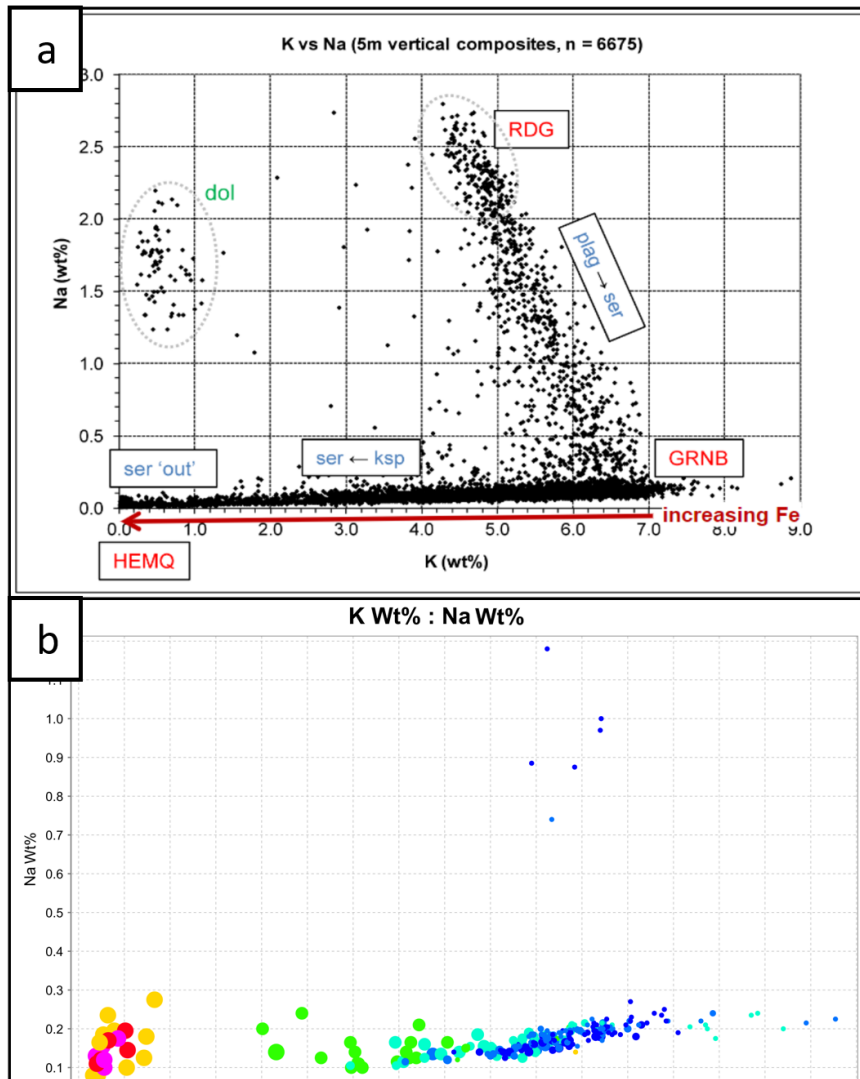
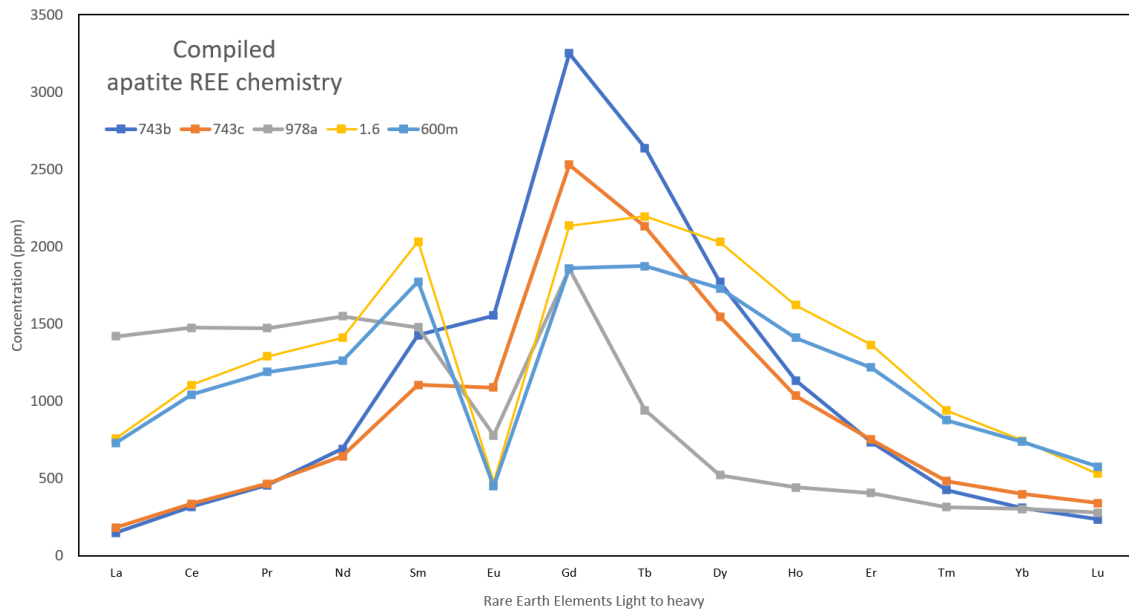


Figure 19. Alkali elements comparison. (a) IOCG Olympic Dam presentation, showing the transition from host granite to granite breccia and into hematite ore (Ehrig 2013). RDG- Roxby Downs granite, GRNB -granite breccia, and HEMQ Hematite ore (b) Alkali element Plot Na:K, for CAR2038 Drillhole bulk rock geochemistry, colouration mapped to hematite concentration (pink elevated Fe, blue Depleted Fe). And point size mapped to distance from deposit (large close, small far).

Apatite from this report were seen in predominantly two groups, a uniform and consistent group which are related to the granite, and more heterogenous and dispersed group which seem to be related to ore-forming fluids and brecciation. To further assess this, a comparison with previous trace element work can be made which also investigated apatite and trace/REEs (North 2020).

Figure 20 shows the granite samples in this study (1.6m, 600m) have a similar REE signature, with enrichment in the middle REEs and a notable negative Eu anomaly. This anomaly is shared by the 978a sample, which was inferred as a granite raft within the ore breccia. Apatite from the nearby-Olympic Dam have been inferred as hydrothermal-infilling, based on a positive Eu anomaly, with magmatic apatite's related to a negative Eu anomaly (Krneta 2017). This would infer with more confidence that the apatite seen in the granite, (from 1.6m - ~700m) have preserved an age which predates mineralisation, and their REE signature disassociates them from the hydrothermal events of the deposit formation.



**Figure 20. Apatite chondrite normalised-REE chemistry from trace element analysis of LA-ICP-MS. Orange, dark blue and grey from (North 2020), averaged apatite composition from different areas of the ore zone (spatial information seen in Appendix K). Yellow and light blue trends from this study, from CAR2038 in the ‘Donington Suite’. All apatite exhibit a middle-REE enrichment. 1.6, 600m and 978a all contain granite more than hematite, and all exhibit a depletion in Europium. Granite samples have a more diverse distribution of REE.**

Ca has ionic radius and charge similar to Eu and therefore will occasionally be replaced by it (Dyger 2020). Minerals such as plagioclase take up a lot of the available Ca and subsequently Eu. If plagioclase is crystallising, it may take the Eu with it (more than any other REE)- negative anomaly. Eu is the most volatile of the REE-series, reacting with water and dilute acids, which would suggest that hydrothermal fluids moving through the host rock were at least partly acidic. This trend has also been seen in other deposits, where the hydrothermal alteration of granite, with dissolution of K-feldspar, is connected to a prominent negative Eu anomaly (René 2012).

## 6. CONCLUSIONS

The Carrapateena deposit offers insight into the characteristic hydrothermal alteration of IOCG deposits across the Olympic Cu-Au province. Geochemistry, petrographic observations, and geochronology from this study support the following conclusions:

1. The alteration system of Carrapateena is an interplay between an older regional alteration texture of low temperature hydrothermal alteration, represented by chlorite, overprinted by more intensive hydrothermal alteration. Characteristic alteration is seen as the relationship between hematite in the deposit, sericite affecting the fringe of the deposit and CBC, and chlorite affecting most of the regional host rock.
2. Monazite, zircon and xenotime support the host granite relating to the accepted age of Donington Suite, further affirming the expected age of host rock for Carrapateena, with characteristic alteration as described, predominately chlorite altered.
3. Data for ~1780Ma aged events, recorded within the altered chlorite and sericite, potentially linked to an intermediate stage of alteration. Apatite and zircon have supported the consideration of Wallaroo Group/McGregor Volcanics timing for alteration of the Donington Suite granite (Pre-dating CBC events).
4. The extent of alteration 'halos' is not very applicable in this deposit-study, as the changes in composition were typically found as abrupt as the transition into the CBC itself, with regional scale alteration of chlorite potentially linked to events which predates the ore-system. The lack of preserved 'halos' as discussed could relate more to differing systems encountered, rather than a progressive change along the drillhole.

## 7. FURTHER STUDY

To better understand the timing of the replacement mineral sericite, Rb-Sr dating could be implemented to assess the mineral history. By better understanding when sericite formed in the deposit, better context for the alteration history can be explained. As discussed, the apatite in the granite preserves an intermediate age between the host rock and deposit, the Rb-Sr dating could distinguish if the age is due to regrowth or thermal partial resetting. Currently it is assumed that the hematite veining and breccia mass happened synchronously with the alteration of chlorite to sericite. However, this assumption could be proven false and would then potentially show that the feldspar-chlorite reaction may be an older texture which is merely preserved where the hematite is coincidentally.

The 2-Dimensional analysis of distal-proximal relationships investigated here does not have supporting evidence for any other directions around the ore deposit. Especially given the suggestion of fault activity masking the alteration affects recorded by the host granite as discussed in apatite geochronology. More investigation on all sides of the deposit could distinguish whether this preservation is seen in all directions, or if there is a fault relationship that has displaced the affected granite.

## **ACKNOWLEDGMENTS**

Thank you to my supervisor Dr. Richard Lilly and co-supervisor Prof. Martin Hand for their expertise, career coaching, support and guidance at Adelaide University throughout the year. To Mitch Neumann and Shaun Light at OZ Minerals, thank you for providing technical and logistical support. To the Playford Trust and AusIMM, thank you for both generous financial and career related support. Thanks to Aoife McFadden, Sarah Gilbert and Benjamin Wade for assisting and teaching with all Adelaide microscopy related work and analyses. Thanks to PhDs Mitchell Bockmann, Brad Cave and Sam March for providing advice and guidance. Finally a big thank you to the Honours cohort for making the year so interesting and enjoyable.



## REFERENCES

- APUKHTINA, O., KAMENETSKY, V., EHRIG, K., KAMENETSKY, M., MAAS, R., THOMPSON, J., MCPHIE, J., CIOBANU, C., & COOK, N. (2017). Early, Deep Magnetite-Fluorapatite Mineralization at the Olympic Dam Cu-U-Au-Ag Deposit, South Australia. *Economic Geology and the Bulletin of the Society of Economic Geologists*, 112(6), 1531–1542.
- BELPERIO, A., FLINT, R., & FREEMAN, H. (2007). Prominent Hill: A Hematite-Dominated, Iron Oxide Copper-Gold System. *Economic Geology*, 102(8), 1499–1510
- BOWDEN, B., FRASER, G., DAVIDSON, G., MEFFRE, S., SKIRROW, BULL, S. & THOMPSON, J. (2017). Age constraints on the hydrothermal history of the Prominent Hill iron oxide copper-gold deposit, South Australia. *Mineralium Deposita*, 52(6), 863–881.
- BROTODEWO A., et al. 2021 Geochemical discrimination of igneous zircon in the Gawler Craton, South Australia, *Australian Journal of Earth Sciences*, vol. 68, no. 4, pp. 557-579.
- CHAPMAN N. D., 2019 Pb-isotopic constraints on the source of A-type Suites: Insights from the Hiltaba Suite - Gawler Range Volcanics Magmatic Event, Gawler Craton, South Australia, *Lithos*, vol. 346-347, p. 105156.
- CHERRY, A., KAMENETSKY, V., MCPHIE, J., KAMENETSKY, M., EHRIG, K., & KEELING, J. (2017). Post 1590 Ma modification of the supergiant Olympic Dam deposit: links with regional tectonothermal events. In *Proceedings, 14th SGA Biennial Meeting 'Mineral Resources to Discover'*, Québec City, QC, Canada, 20-23.
- CHERRY, A., KAMENETSKY, V., MCPHIE, J., THOMPSON, J., EHRIG, K., MEFFRE, S., KAMENETSKY, M & KRNETA, S. (2018). Tectonothermal events in the Olympic IOCG Province constrained by apatite and REE-phosphate geochronology. *Australian Journal of Earth Science*, 65(5), 643-659.
- CORRIVEAU, L & POTTER, E. (2019). Alteration facies in 'IOCG terranes': a global view on mineral systems with IOCG and affiliated deposit types. *Geological Survey of South Australia*, 1-33.
- COURTNEY-DAVIES L., et al. 2019 Hematite geochemistry and geochronology resolve genetic and temporal links among iron-oxide copper gold systems, Olympic Dam district, South Australia, *Precambrian Research*, vol. 335, p. 105480.
- COWLEY, W., CONOR, C & ZANG, W. (2003). New and revised Proterozoic stratigraphic units on northern Yorke Peninsula. *MESA Journal*, 29, 46–58.
- CURTIS S. 2012 The Cooyerdoo Granite: Mesoarchaean basement of the Gawler Craton, *MESA Journal*, vol. 65, pp. 31-40.
- DALY, S. (1998). Tectonic evolution and exploration potential of the Gawler Craton, South Australia. *AGSO J. Aust. Geol. Geophys.*, 17, 145-168.
- DAVIDSON, G., PATERSON, H., MEFFRE, S., & BERRY, R. (2007). Characteristics and Origin of the Oak Dam East Breccia-Hosted, Iron Oxide Cu-U-(Au) Deposit: Olympic Dam Region, Gawler Craton, South Australia. *Economic Geology*, 102(8), 1471–1498.
- DEL REAL., et al. 2021 Formation of giant iron oxide-copper-gold deposits by superimposed, episodic hydrothermal pulses, *Communications Earth & Environment*, vol. 2, no. 1, p. 192.
- DIREEN, N.G., LYONS, P., 2007, Regional crustal setting of iron oxide Cu-Au mineral systems of the Olympic Dam region, South Australia: Insights from potential-field modelling.: *Society of Economic Geologists*, v. 102, p. 1397-1414.
- DMITRIJEVA, M., CIOBANU, C. L., EHRIG, K., COOK, N, METCALFE, A, VERDUGO-IHL, M, & MCPHIE, J. (2019). Mineralization-alteration footprints in the Olympic Dam IOCG district, South Australia: The Acropolis prospect. *Journal of Geochemical Exploration*, 205. doi:10.1016/j.gexplo.2019.106333
- DYGERT N., et al. 2020 Experimental determinations of trace element partitioning between plagioclase, pigeonite, olivine, and lunar basaltic melts and an fO<sub>2</sub> dependent model for plagioclase-melt Eu partitioning, *Geochimica et Cosmochimica Acta*, vol. 279, pp. 258-280.
- EGGLETON R. A. & BANFIELD J. F. 1985 The alteration of granitic biotite to chlorite, *American Mineralogist*, vol. 70, no. 9-10, pp. 902-910.
- EHRIG K, 2013, *Geology and Mineralogical Zonation of the Olympic Dam Fe-oxide Cu-U-Ag Deposit*, bhpbilliton.
- FERRIS, G. M., SCHWARZ, M. P., & HEITHERSAY, P. (2002). The geological framework, distribution and controls of Fe-oxide Cu-Au mineralisation in the Gawler Craton, South Australia. Part I– Geological and tectonic framework. *Hydrothermal iron oxide copper-gold and related deposits: A global perspective*, 2, 9-31.

- FRASER G., et al. 2010 Discovery of early Mesoproterozoic crust in the eastern Gawler Craton, South Australia, *Precambrian Research*, vol. 179, pp. 1-21.
- GUSTAFSON, L. & COMPSTON, W. (1979). Rb-Sr dating of Olympic Dam core samples, Report to Western Mining Corporation, Research School of Earth Sciences, Australian National University, 18.
- HALL J. W., et al. 2018 Thermal history of the northern Olympic Domain, Gawler Craton; correlations between thermochronometric data and mineralising systems, *Gondwana Research*, vol. 56, pp. 90-104.
- HAND, M., REID, A & JAGODZINSKI, L. (2007). Tectonic framework and evolution of the Gawler Craton, southern Australia. *Society of Economic Geologists Inc*, 102, 1377-1395.
- HAYWARD, N., & SKIRROW, R. (2010). Geodynamic setting and controls on iron oxide Cu-Au ( $\pm$ U) ore in the Gawler Craton, South Australia. In: *Hydrothermal Iron Oxide Copper-Gold and Related Deposits: A global Perspective*, 3, 119-146.
- HITZMAN, M, ORESKES, N & EINAUDI, M. (1992). Geological characteristics and tectonic setting of Proterozoic iron oxide (Cu-U-Au-REE) deposits. *Precambrian Research*, 58, 241-287.
- HELLSTROM, J., PATON, C., WOODHEAD, J. D. & HERGT, J. Iolite: Software for spatially resolved LA-(QUAD and MC)-ICP-MS analysis. *Mineral. Assoc. Canada Short Course Ser.* 40, 343-348 (2008)
- JACKSON, S. E., PEARSON, N. J., GRIFFIN, W. L., & BELOUSOVA, E. A. (2004). The application of laser ablation-inductively coupled plasma-mass spectrometry to in situ U-Pb zircon geochronology. *Chemical Geology*, 211(1), 47-69.
- JAGODZINSKI EA, REID AJ, CHALMERS N, SWAIN G, FREW RA, FOUODOULIS C (2007) Compilation of SHRIMP U-Pb geochronological data for the Gawler Craton, South Australia, 2007. Department of Primary Industries and Resources Report Book 2007/2
- KIRKLAND C. L., et al. 2018 Apatite: a U-Pb thermochronometer or geochronometer?, *Lithos*, vol. 318-319, pp. 143-157.
- KONTONIKAS-CHAROS A., ET AL. 2017 Feldspar evolution in the Roxby Downs Granite, host to Fe-oxide Cu-Au(U) mineralisation at Olympic Dam, South Australia, *Ore Geology Reviews*, vol. 80, pp. 838-859.
- KRNETA, S., CIOBANU, C., COOK, N., EHRIG, K., & KONTONIKAS-CHAROS, A. (2017b). Rare Earth Element Behaviour in Apatite from the Olympic Dam Cu-U-Au-Ag Deposit, South Australia. *Minerals*, 7(8).
- KRNETA, S., COOK, N., CIOBANU, C., EHRIG, K., & KONTONIKAS-CHAROS, A. (2017a). The Wirrda Well and Acropolis prospects, Gawler Craton, South Australia: Insights into evolving fluid conditions through apatite chemistry. *Journal of Geochemical Exploration*, 181, 276-291. <https://doi.org/10.1016/j.gexplo.2017.08.004>
- LANE, K., JAGODZINSKI, E., DUTCH R., REID, A & HAND M. (2015). Age constraints on the timing of iron ore mineralisation in the southeastern Gawler Craton. *Australian Journal of Earth Sciences*, 62(1), 55-75.
- LISA VELLA & MICHAEL CAWOOD (2012) Geophysical Characteristics of the Carrapateena Iron-Oxide Copper-Gold Deposit, *ASEG Extended Abstracts*, 2012:1, 1-4, DOI:10.1071/ASEG2012ab160
- MAAS, R., KAMENETSKY, V., EHRIG, K., MEFFRE, S., MCPHIE, J., & DIEMAR, G. (2011). Olympic Dam U-Cu-Au deposit, Australia: New age constraints. *Mineralogical Magazine*, 75, 1375.
- MCINNES, B., KEAYS, R., LAMBERT, D., HELLSTROM, J., & ALLWOOD, J. (2008). Re-Os geochronology and isotope systematics of the Tanami, Tennant Creek and Olympic Dam Cu-Au deposits. *Australian Journal of Earth Sciences*, 55(6-7), 967-981.
- MCPHIE, J., EHRIG, K., KAMENETSKY, M., CROWLEY, J., & KAMENETSKY, V. (2020). Geology of the Acropolis prospect, South Australia, constrained by high-precision CA-TIMS ages. *Australian Journal of Earth Sciences*, 1-18.
- MCPHIE, J., KAMENETSKY, V., ALLEN, S., EHRIG, K., AGANGI, A., & BATH, A. (2011). The fluorine link between a supergiant ore deposit and a silicic large igneous province. *Geology*, 39(1), 1003-1006.
- MCPHIE J., et al. 2011 Origin of the supergiant Olympic Dam Cu-U-Au-Ag deposit, South Australia: Was a sedimentary basin involved?, *Geology*, vol. 39, no. 8, pp. 795-798.

- NORTH, B. (2020). The Geochemistry of Rare Earth Element-Bearing Minerals and their Relationship to Copper Sulphide Mineralisation at the Carrapateena Deposit, South Australia, Adelaide University-OZ minerals thesis.
- NUEMANN, M (2019). IOCG Workshop – Gawler Craton, Stuart Shelf hematite rich end members. Project Exploration Geologists, OZ Minerals.
- OZ Minerals. (2019). Carrapateena 2019 mineral resources and ore reserves statement and explanatory notes. Public report to the ASX, 30/06/2019, 1-56.
- PARKER, A.J., LEMON, N.M., 1982, Reconstruction of the Early Proterozoic stratigraphy of the Gawler Craton, South Australia, Geological Society of Australia. Journal, 29(2), p221-23
- PATON C., et al. 2011 Iolite: Freeware for the visualisation and processing of mass spectrometric data, Journal of Analytical Atomic Spectrometry, vol. 26, no. 12, pp. 2508-2518.
- PAYNE J. L., et al. 2008 Temporal constraints on the timing of high-grade metamorphism in the northern Gawler Craton: implications for assembly of the Australian Proterozoic, Australian Journal of Earth Sciences, vol. 55, no. 5, pp. 623-640.
- PORTER, T. (2010). The Carrapateena iron oxide copper gold deposits, Gawler Craton, South Australia: A review. In: Hydrothermal Iron Oxide Copper-Gold and Related Deposits: A global Perspective, 3, 191- 200.
- PREISS, W., 2000, The Adelaide Geosyncline of South Australia and its significance in Neoproterozoic continental reconstruction.: Precambrian Research, v. 100, p. 21
- REID, A. (2019). The Olympic Cu-Au Province, Gawler Craton: A Review of the Lithospheric Architecture, Geodynamic Setting, Alteration Systems, Cover Successions and Prospectivity. Minerals, 9( 6), 1-371.
- REID, A. J., et al. Report Book (2016) Department of State Development. Magmatic processes of the St Peter Suite, Gawler Craton: new U-Pb geochronological data and field observations.
- REID A. J. & FABRIS A. 2015 Influence of Preexisting Low Metamorphic Grade Sedimentary Successions on the Distribution of Iron Oxide Copper-Gold Mineralization in the Olympic Cu-Au Province, Gawler Craton\*, Economic Geology, vol. 110, no. 8, pp. 2147-2157.
- REEVE, J.S., CROSS, K.C., SMITH, R.N., ORESKES, N., 1990, Olympic Dam Copper-Uranium-Gold-Silver Deposit.: In Geology of the Mineral Deposits of Australia and Papua New Guinea, p. 1009-1095.
- SAWYER, M., WHITTAKER, B & DELITTLE, J. (2017). Carrapateena Iron Oxide Copper-Gold-Silver-Uranium Deposit. Australian Ore Deposits. AusIMM.
- SCHNEIDER, C. A., RASBAND, W. S., & ELICEIRI, K. W. (2012). NIH Image to ImageJ: 25 years of image analysis. Nature Methods, 9(7), 671–675. doi:10.1038/nmeth.2089
- SCHOENE, B., & BOWRING, S. A. (2006). U–Pb systematics of the McClure Mountain syenite: thermochronological constraints on the age of the 40Ar/39Ar standard MMhb. Contributions to Mineralogy and Petrology, 151, 615-630. doi:10.1007/s00410-006- 0077-4
- SHA L.-K. & CHAPPELL B. W. 1999 Apatite chemical composition, determined by electron microprobe and laser-ablation inductively coupled plasma mass spectrometry, as a probe into granite petrogenesis, Geochimica et Cosmochimica Acta, vol. 63, no. 22, pp. 3861-3881.
- SKIRROW, R., Bastrakov, E., Davidson, G., Raymond, O., & Heithersay, P. (2002). The geological framework, distribution and controls of Fe-oxide Cu-Au mineralisation in the Gawler Craton, South Australia. Part II-alteration and mineralisation
- SWAIN, G., Woodhouse, A., Hand, M., Barovich, K., Schwarz, M., Fanning, C.M., 2005a, Provenance and tectonic development of the late Archean Gawler craton, Australia: U-Pb zircon, geochemical and Sm-Nd isotopic implications. Precambrian Research, v. 141, p. 106-136
- TAPPERT M. C., et al. 2013 The mineral chemistry, near-infrared, and mid-infrared reflectance spectroscopy of phengite from the Olympic Dam IOCG deposit, South Australia, Ore Geology Reviews, vol. 53, pp. 26-38.
- TAYLOR, R. (2014). Paragenesis, ore textures and general observations, Carrapateena prospect. from Tasmania (internal report)
- THOMSON, S. N., GEHRELS, G. E., RUIZ, J., & BUCHWALDT, R. (2012). Routine low-damage apatite U-Pb dating using laser ablation–multicollector–ICPMS. Geochemistry, Geophysics, Geosystems, 13(2). doi:10.1029/2011GC003928
- TIDDY C. 2021 Monazite as an Exploration Tool for Iron Oxide-Copper-Gold Mineralisation in the Gawler Craton, South Australia, Minerals, vol. 11, no. 8.
- VELLA, L & EMERSON, D. (2009). Carrapateena: Physical properties of a new iron-oxide copper-gold deposit. (internal report).

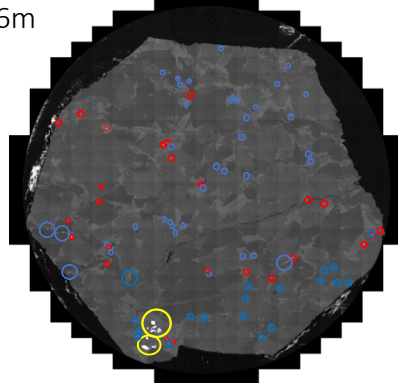
WILLIAMS P. (2012). Comments on Carrapateena Geology from Inspection of CAR075, CMG\_27/1  
(internal report).

### Appendix A: Extended LA-ICP MS Methodology

In this study, two runs of monazite apatite and xenotime, and a single run of zircon, were analysed by laser ablation mass spectrometry at Adelaide microscopy. Laser spots were positioned to achieve a consistent number of analysis on each crystal within a sample. Prior to LA-ICP MS analysis all minerals were identified through AMICS and BSE-XRF, then imaged by BSE and Cathodoluminescences, all on the Hitachi 3800 SEM. With planned targets for granite samples seen below.

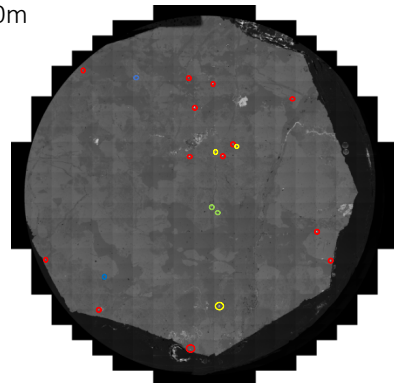
Granite 1.6m  
BSE

• 100micro  
Red-Zircon  
Blue-Apatite  
Green-Xenotime  
Yellow-Monazite



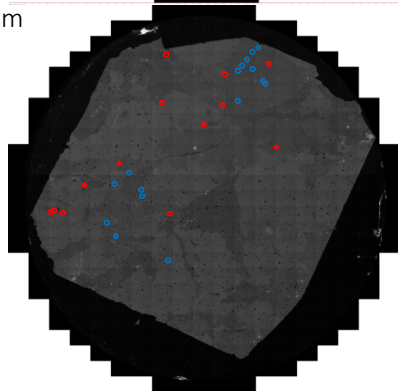
Granite 300m  
Vined  
BSE

• 100micron  
Red-Zircon  
Blue-Apatite  
Green-Xenotime  
Yellow-Monazite



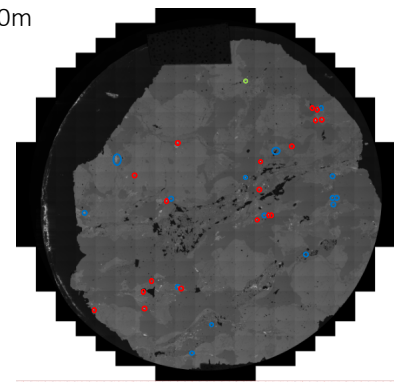
Granite 300m  
Alt  
BSE

• 100micron  
Red-Zircon  
Blue-Apatite  
Green-Xenotime  
Yellow-Monazite



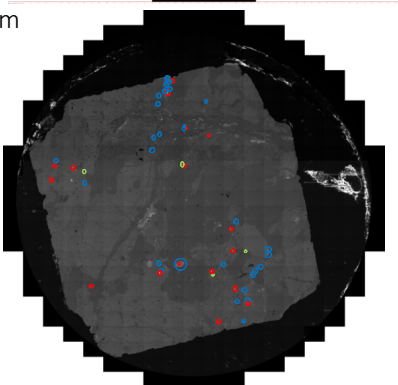
Granite 600m  
Vined  
BSE

• 100micron  
Red-Zircon  
Blue-Apatite  
Green-Xenotime  
Yellow-Monazite



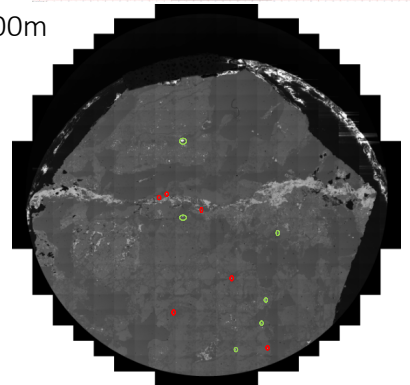
Granite 600m  
Alt  
BSE

• 100micron  
Red-Zircon  
Blue-Apatite  
Green-Xenotime  
Yellow-Monazite



Granite 700m  
BSE


• 100micron  
Red-Zircon  
Blue-Apatite  
Green-Xenotime  
Yellow-Monazite



Appendix B: Extended petrography reports

Petrographic observations made to build understanding of characteristic textures between alteration minerals and the affected host granite minerals.

**EG20CAR2038**  
**1.6m**




TS Summary:

- **Main Clasts/Phenocrysts**  
Quartz, k-feldspar, Biotite, Sericite
- **Vein and infill textures**  
Dominant vein 2mm wide calcite vein
- **Alteration Assemblage/texture**  
Chlorite dominant, chlorite replacing biotite most heavily in contact with feldspars.
- **Notable comments**  
Orthogonal veining texture seen within some feldspars.

**AMICS sample**  
**Estimated area**

Name	Area %
Quartz	30.00%
Orthoclase	28.00%
Sericite	19.00%
Chlorite	6.00%
Albite	5.00%
Biotite	4.50%
Carbonates	0.60%
Apatite	0.20%
Rutile	0.07%
Zircon	0.02%
Monazite	0.02%
Hematite	0.00%

**EG20CAR2038**  
**300m**



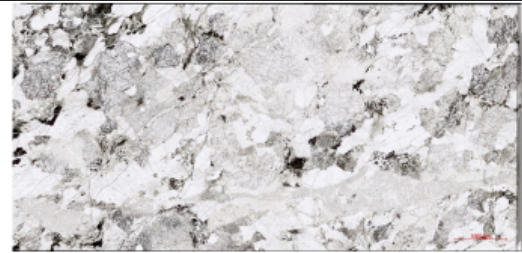
TS Summary:

- **Main Clasts/Phenocrysts**  
Megacrysts of k-feldspar (multiple twinning), smaller phenocrysts of quartz
- **Vein and infill textures**  
Sericite crosscuts megacrysts
- **Alteration Assemblage/texture**  
Sericite-chlorite replace biotite k-spar
- **Notable comments**  
"cross hatching" feldspars, sericite/ chlorite along planes within feldspars

**AMICS sample**  
**Estimated area**

Name	Area%
Quartz	33.57
Orthoclase	47.36
Sericite	14.12
Chlorite	0.03
Albite	0.01
Biotite	0.16
Apatite	0.07
Zircon	0.01
Monazite	0
Hematite	0

EG20CAR2038  
 600m



TS Summary:

- **Main Clasts/Phenocrysts**  
 Phenocrysts of quartz and K-feldspars,  
 More quartz than feldspars
- **Vein and infill textures**  
 Calcite vein,
- **Alteration Assemblage/texture**  
 Sericite and chlorite wrapping and  
 replacing feldspars
- **Notable comments**  
 Fine cross hatching of feldspars

AMICS sample  
 Estimated area

Name	Area%
Quartz	42.3
Orthoclase	27.86
Sericite	20.71
Chlorite	0.14
Albite	0.01
Biotite	0.34
Apatite	0.2
Zircon	0.03
Monazite	0
Hematite	0.1

EG20CAR2038  
 700m



TS Summary:

- **Main Clasts/Phenocrysts**  
 Mostly quartz phenocrysts and altered  
 feldspars
- **Vein and infill textures**  
 Large hematite bearing veins with fine  
 quartz crystals supported in the vein.
- **Alteration Assemblage/texture**  
 Sericite replacing chlorite and feldspars,  
 from inside crystals
- **Notable comments**

AMICS sample  
 Estimated area

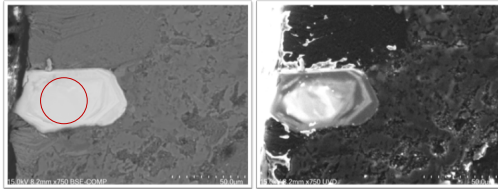
Name	Area %
Quartz	42.00%
Orthoclase	27.00%
Sericite	17.00%
Chlorite	0.17%
Albite	0.00%
Biotite	0.40%
Carbonates	0.00%
Apatite	0.20%
Xenotime	0.01%
Zircon	0.01%
Monazite	0.00%
Hematite	3.00%



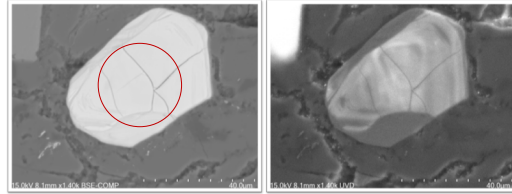
Appendix C SEM BSE and CL

Zircon imaging under BSE and cathodoluminescence produced images as seen below, these images act to summarise some of the zonation seen in zircon in the Donington Suite. Planning before LA-ICP MS was done to ensure the best spot locations for each grain was selected, by avoiding rim+core analyses and minimising overlap with fractures in grains.

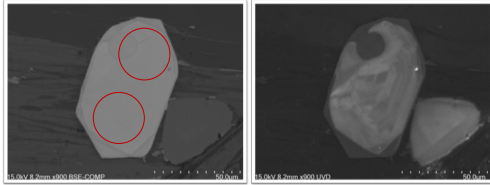
1



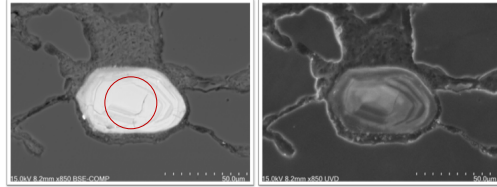
2



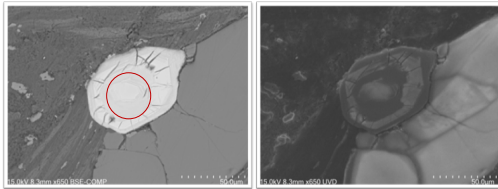
3



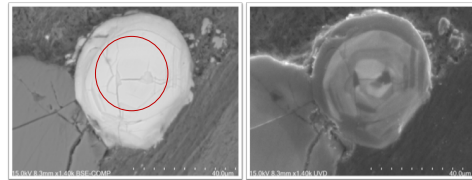
4



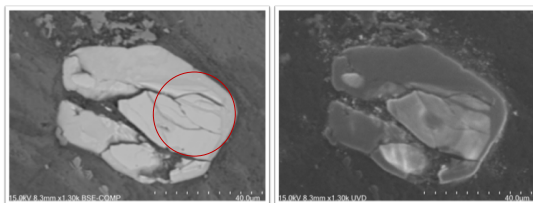
5



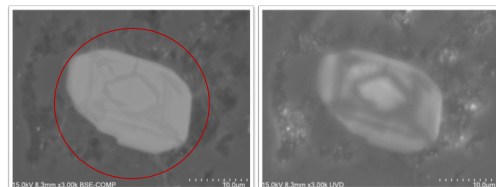
6



7

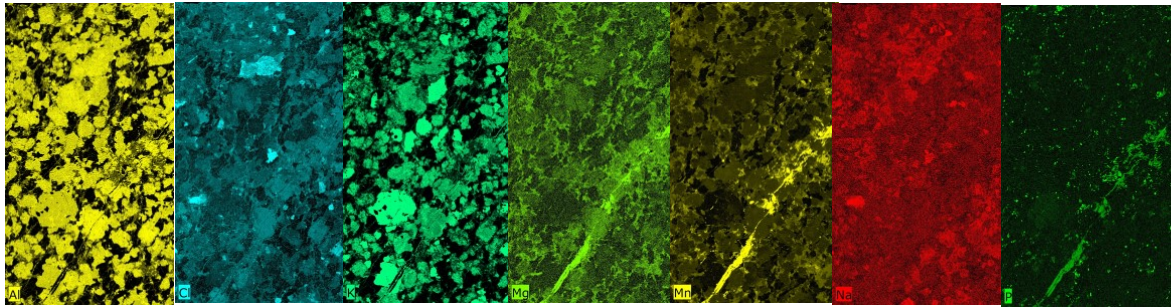


8

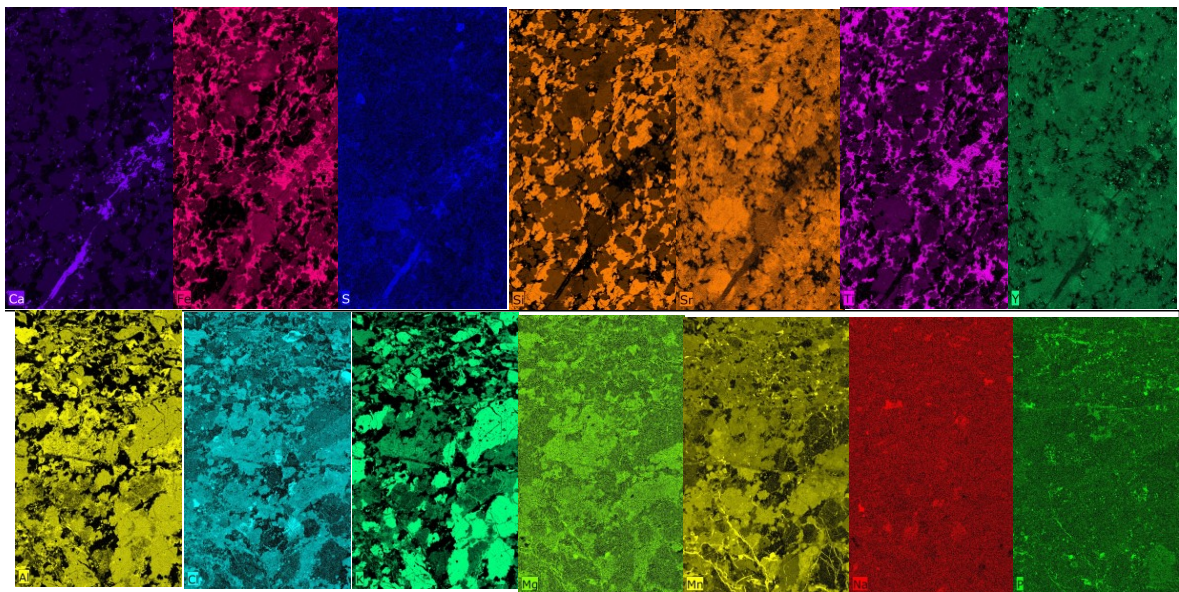




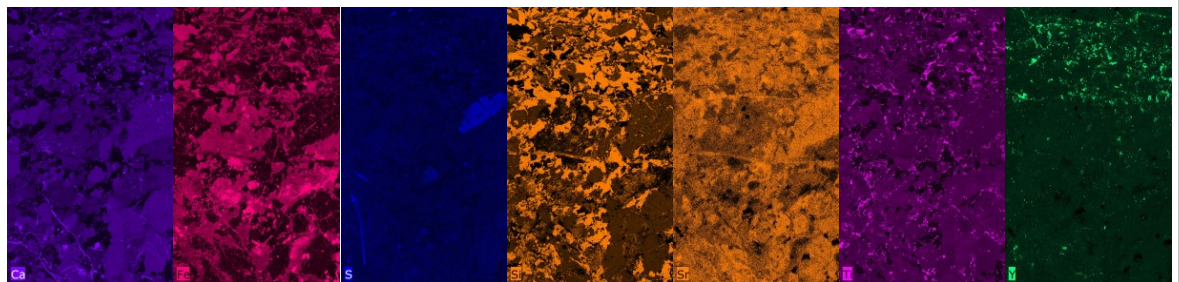
Appendix D: Tornado XRF machine outputs, For Al, Cl, K, Mg, Mn, Na, P, Ca, Fe, S, Si, Sr, Ti and Y respectively.



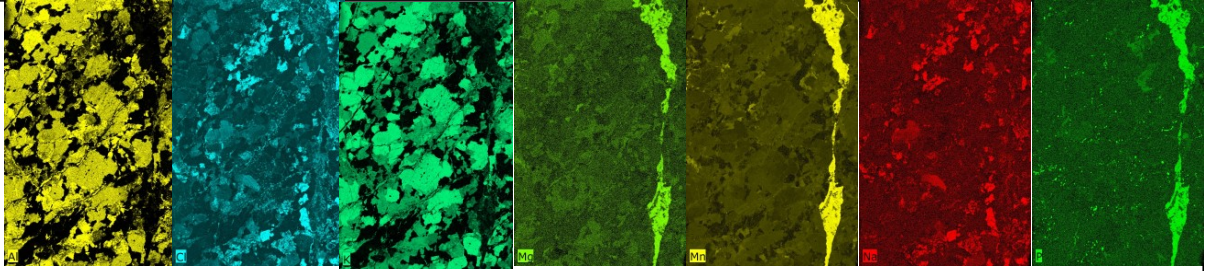
1.6m Granite



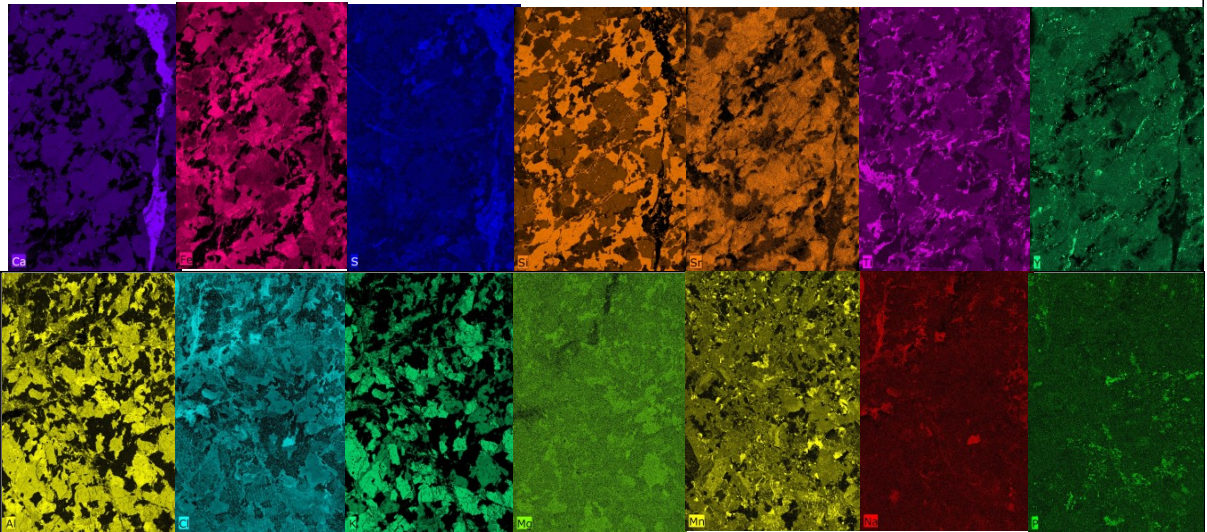
300m granite



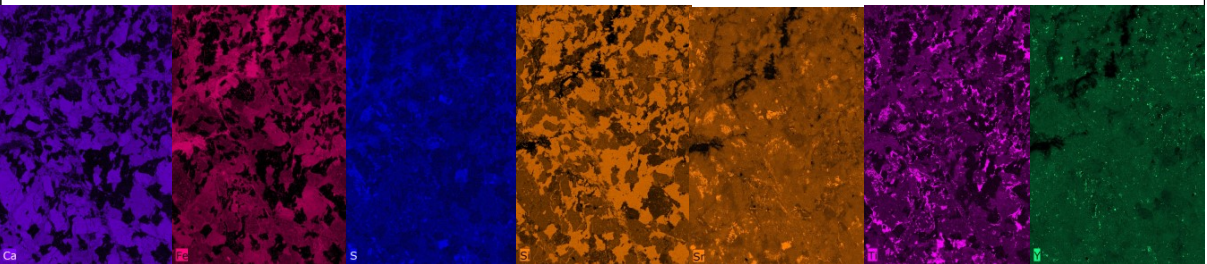




## 600m Granite



## 700m Granite XRF

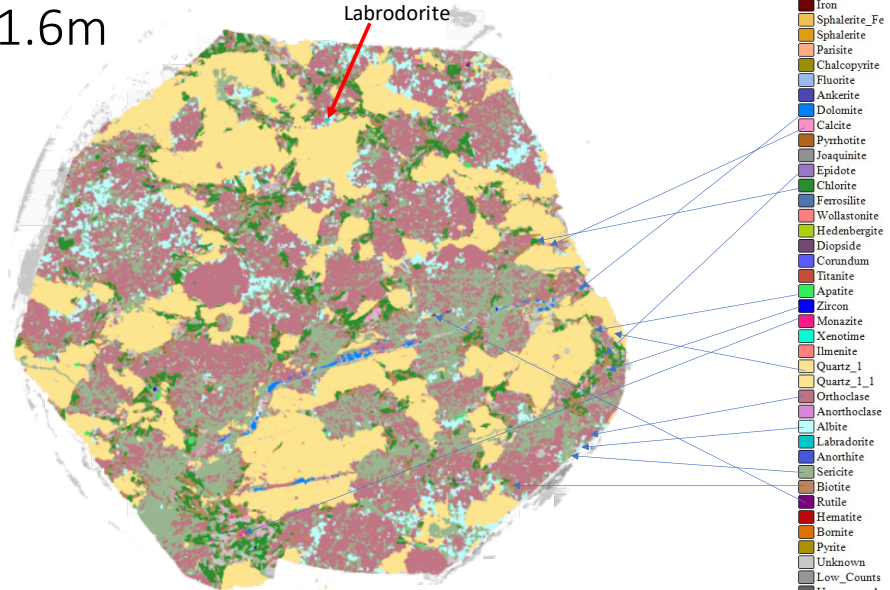


Appendix E: For geochronology, reduction of data reduction followed, for U-Pb isotopes and Trace elements.

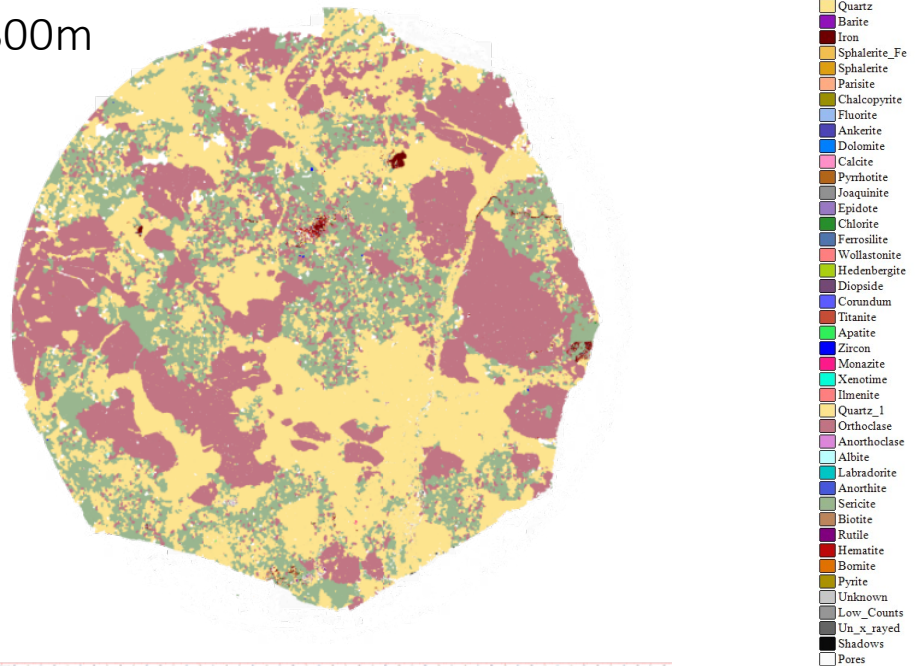
Version 3.6 of Iolite data processing software (Paton et al 2011) was used for xenotime, apatite, monazite, and zircons. This software was selected as it can apply common lead corrections to data. By testing well-constrained standards, this software can correct for the effects of downhole fractionation. Background signal is typically collected by the laser during the first 30 s of data acquisition. This portion of signal should be flat, any spikes that are observed must be removed. A data reduction scheme (DRS) is then applied to create a linear fit to represent the data and then correct for instrumental drift during the analysis. Anomalous data is then excluded to improve the quality of standards, these based on the U-Pb isotopic signals. Bracketing of signals from the unknown analyses was done to ensure only 'flat' signals of fair composition are retained during the data reduction. Finally, the data is exported for both geochronology U-Pb isotopes and for trace elements, with apatite's having a specific DRS for the common lead correction. Exported data is in excel sheets and can be placed into Iolite directly to verify standards (ie Appendix H).

Appendix F: Hitachi 3800-SEM outputted mineral scan, using Bruker-AMICS program to characterise mineral phases and surface areas.

Granite 1.6m  
 AMICS

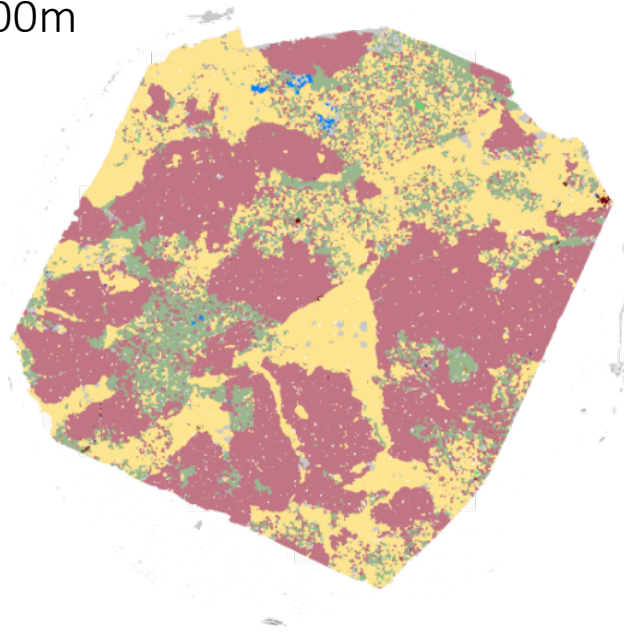


Granite 300m  
 Vined  
 AMICS



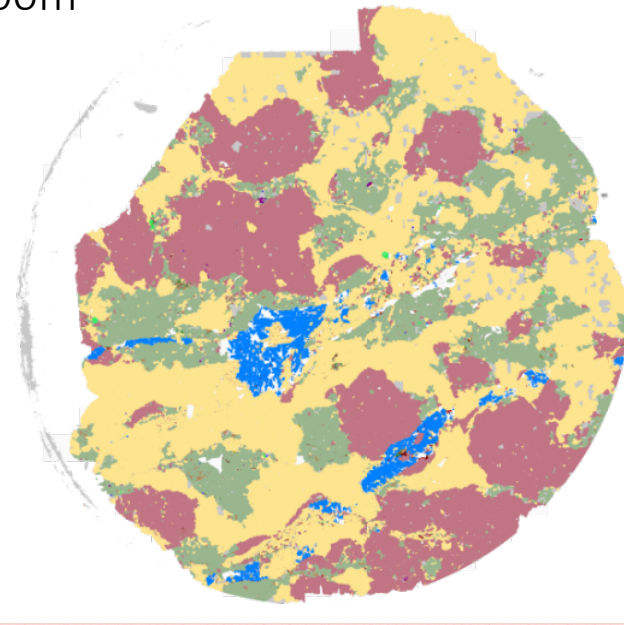


Granite 300m  
Alt  
AMICS



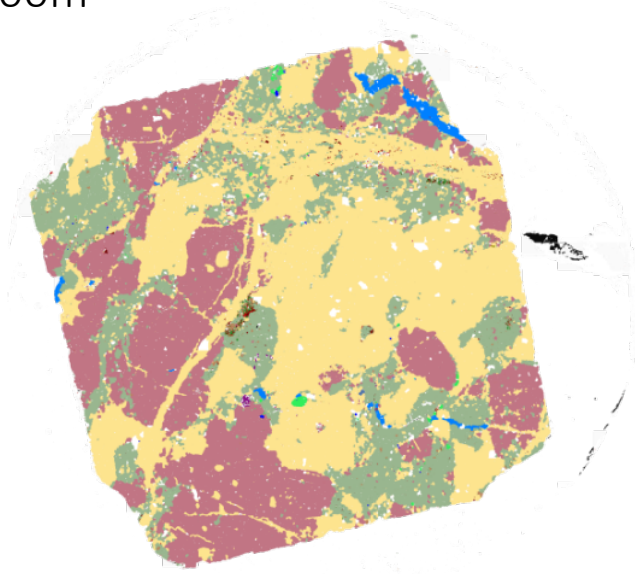
- Quartz
- Barite
- Iron
- Sphalerite\_Fe
- Sphalerite
- Pyrite
- Chalcopyrite
- Fluorite
- Ankerite
- Dolomite
- Calcite
- Pyrrhotite
- Joaquinite
- Epidote
- Chlorite
- Ferrosilite
- Wollastonite
- Hedenbergite
- Diopside
- Corundum
- Titanite
- Apatite
- Zircon
- Monazite
- Xenotime
- Ilmenite
- Quartz\_1
- Orthoclase
- Anorthoclase
- Albite
- Labradorite
- Anorthite
- Sericite
- Biotite
- Rutile
- Hematite
- Bornite
- Pyrite
- Unknown
- Low\_Counts
- Un\_x\_rayed
- Shadows
- Pores

Granite 600m  
Vined  
AMICS

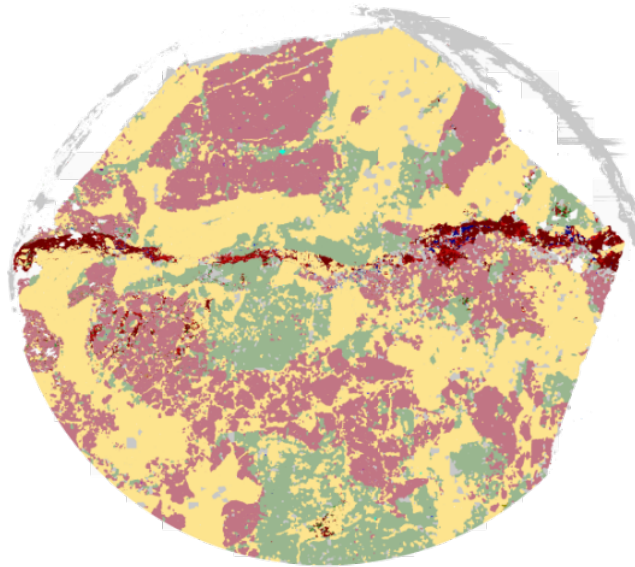


- Quartz
- Barite
- Iron
- Sphalerite\_Fe
- Sphalerite
- Pyrite
- Chalcopyrite
- Fluorite
- Ankerite
- Dolomite
- Calcite
- Pyrrhotite
- Joaquinite
- Epidote
- Chlorite
- Ferrosilite
- Wollastonite
- Hedenbergite
- Diopside
- Corundum
- Titanite
- Apatite
- Zircon
- Monazite
- Xenotime
- Ilmenite
- Quartz\_1
- Orthoclase
- Anorthoclase
- Albite
- Labradorite
- Anorthite
- Sericite
- Biotite
- Rutile
- Hematite
- Bornite
- Pyrite
- Unknown
- Low\_Counts
- Un\_x\_rayed
- Shadows
- Pores

Granite 600m  
 Alt  
 AMICS



Granite 700m  
 AMICS



- Quartz
- Barite
- Iron
- Sphalerite\_Fe
- Sphalerite
- Pyrite
- Chalcopyrite
- Fluorite
- Ankerite
- Dolomite
- Calcite
- Pyrrhotite
- Joaquinite
- Epidote
- Chlorite
- Ferrosilite
- Wollastonite
- Hedenbergite
- Diopside
- Corundum
- Titanite
- Apatite
- Zircon
- Monazite
- Xenotime
- Ilmenite
- Quartz\_1
- Orthoclase
- Anorthoclase
- Albite
- Labradorite
- Anorthite
- Sericite
- Biotite
- Rutile
- Hematite
- Bornite
- Pyrite
- Unknown
- Low\_Counts
- Un\_x\_rayed
- Shadows
- Pores

Appendix G: LA-ICP MS trace element selection filtering for geochronology,

Trace element analysis found in conjunction with U-Pb geochronology of the LA-ICP MS runs was filtered, to avoid contaminated analysis through inaccurate laser spots and inclusions. Identifier elements for target minerals were assessed in comparison to the known standards and secondary standards, the selection of usable data was dictated by the following criteria:

Data for apatite selected by  $\text{Ca} > 35.9 \text{ E}+05 \text{ ppm}$ , and  $< 4.10 \text{ E}05 \text{ ppm}$ , also selected through  $\text{P} > 2.03 \text{ E}05 \text{ ppm}$ , and  $< 2.24 \text{ E}05 \text{ ppm}$ . All data outside this range was considered impure and subsequently was omitted from Terra Wasserberg plots.

Data for xenotimes selected by  $\text{Y} > 5.7 \text{ E}07 \text{ ppm}$  and  $< 7.00 \text{ E}07 \text{ ppm}$ . Data outside this range was omitted from Wetherill plots.

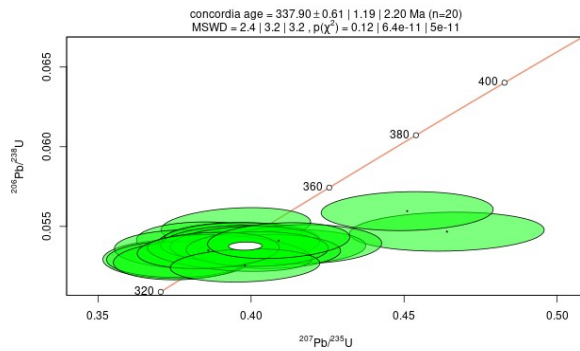
Data for monazites was filtered for  $\text{Ce} < 1.48 \text{ E}08$ , and  $\text{P} > 1.04 \text{ e}05 \text{ ppm}$ . Data from outside this range was excluded (these predominantly were from the Ore-zone, not the Granite).

Zircon data did not require filtering as each tested sample had similar compositions to the reference standards.

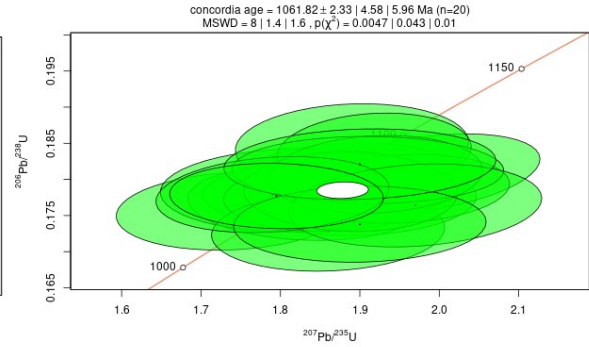
Appendix H: Secondary Standards for verification of analyses taken on both runs.

Zircons, 1<sup>st</sup> run (secondary standards)

Pleisovice (337.13)



91500(1061 lit)

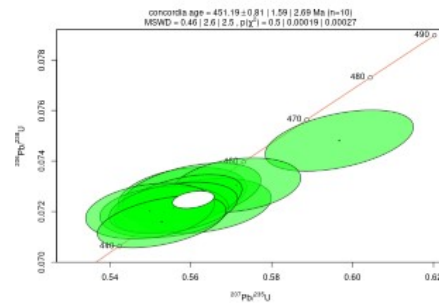
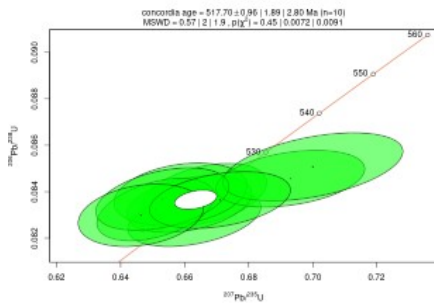


**Iolite: Monazite from 1.6m CAR2038**

U-Pb, Concordia, 2se (abs), 07/35 06/38 07/06, wetheril

Ambat for this run (520-525 lit.)

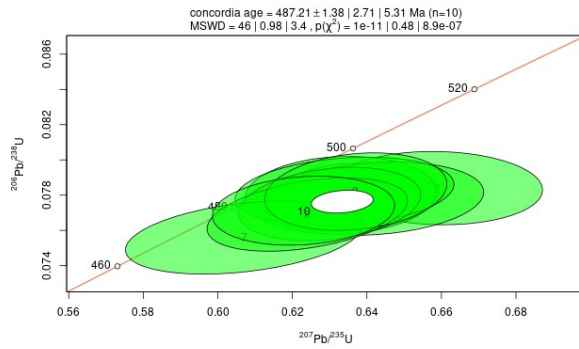
222 for this run (450.2 lit.)





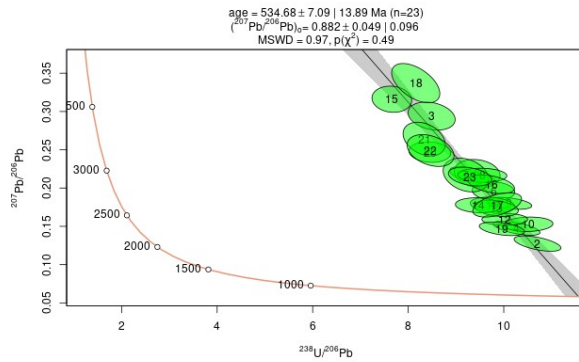
## Xenotime (1<sup>st</sup> run), Secondary standard

MG-1 (490 lit)

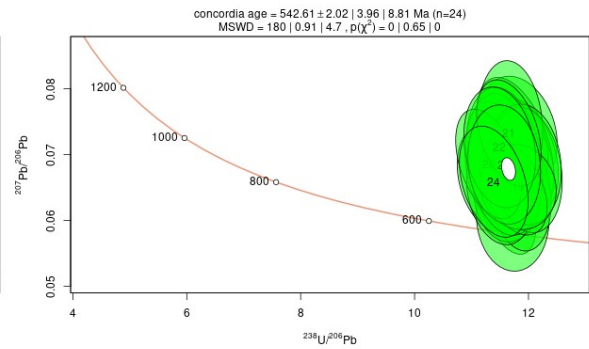


## Apatite (1<sup>st</sup> run) secondary standards

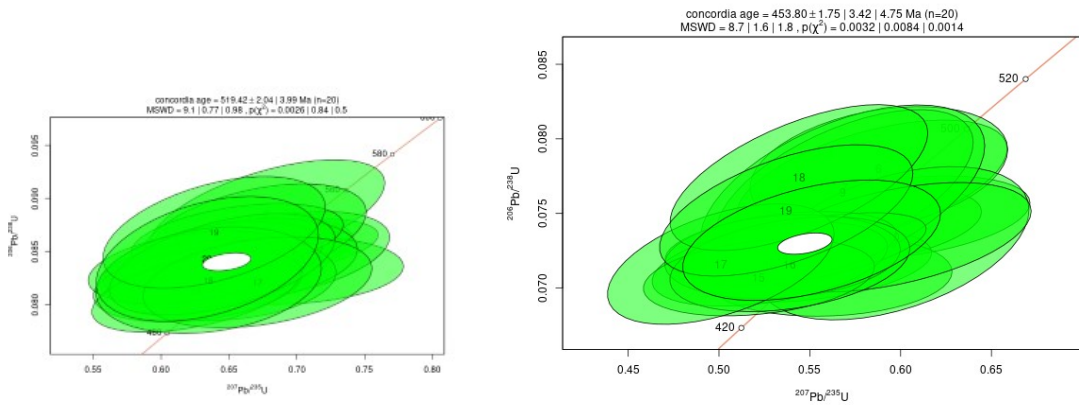
McClure (523.51 Lit)



401 (concordant)(530 lit.)

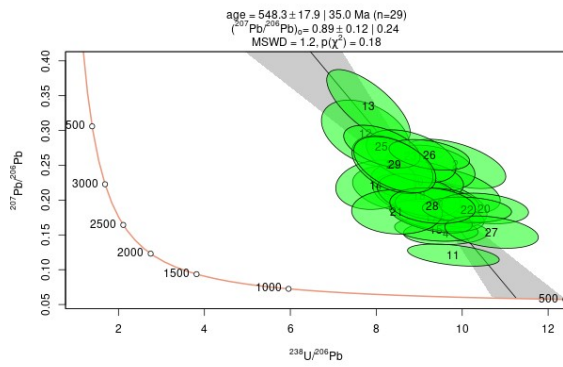


## 2<sup>nd</sup> run- Ore zone Monazite Ambat 222

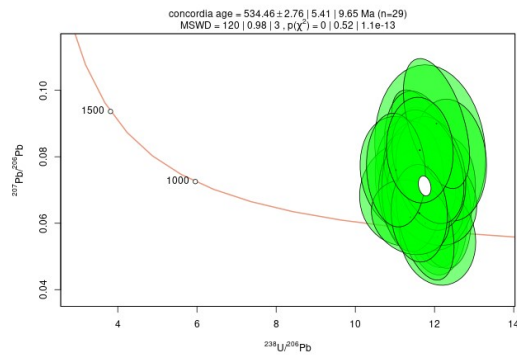


## 2<sup>nd</sup> run apatite (standards)

McClure 525Ma Lit.

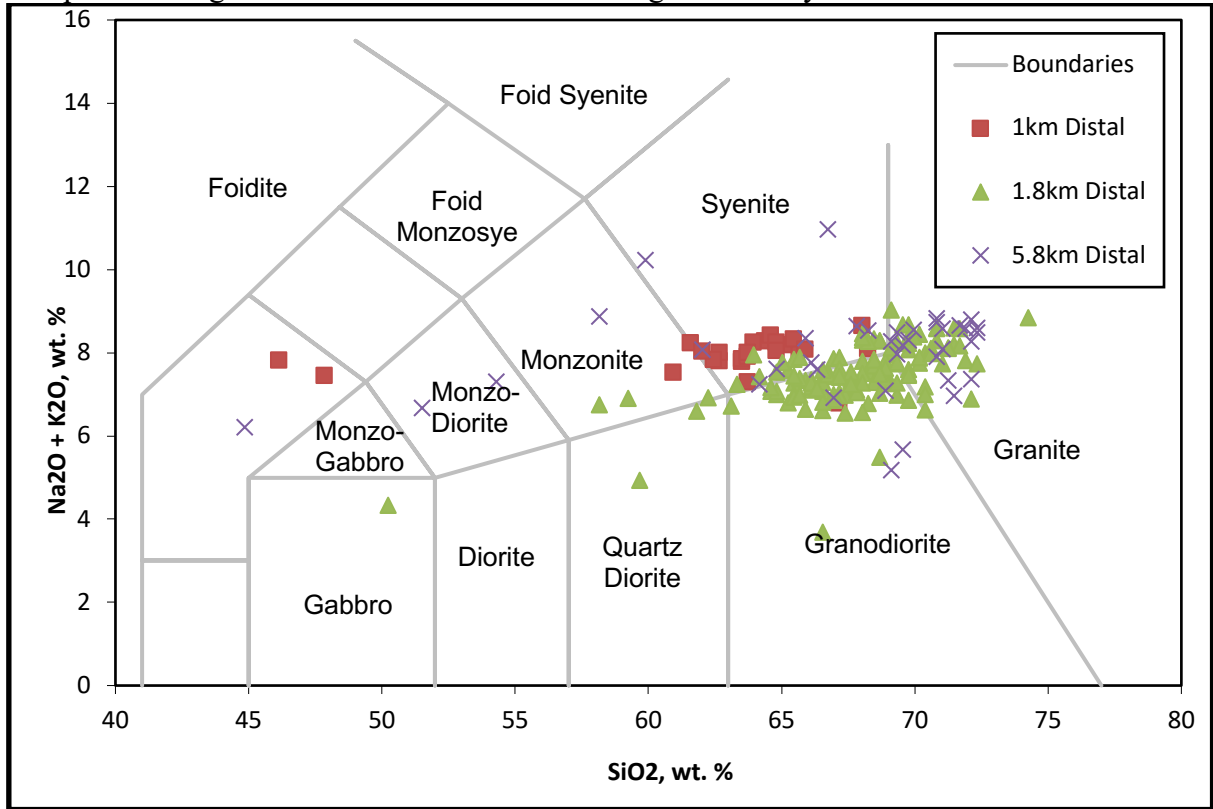


401 530Ma Lit



Appendix J: Granite classification, to verify the probable starting compositions of granite in the Donington Suite granite local to Carrapateena.

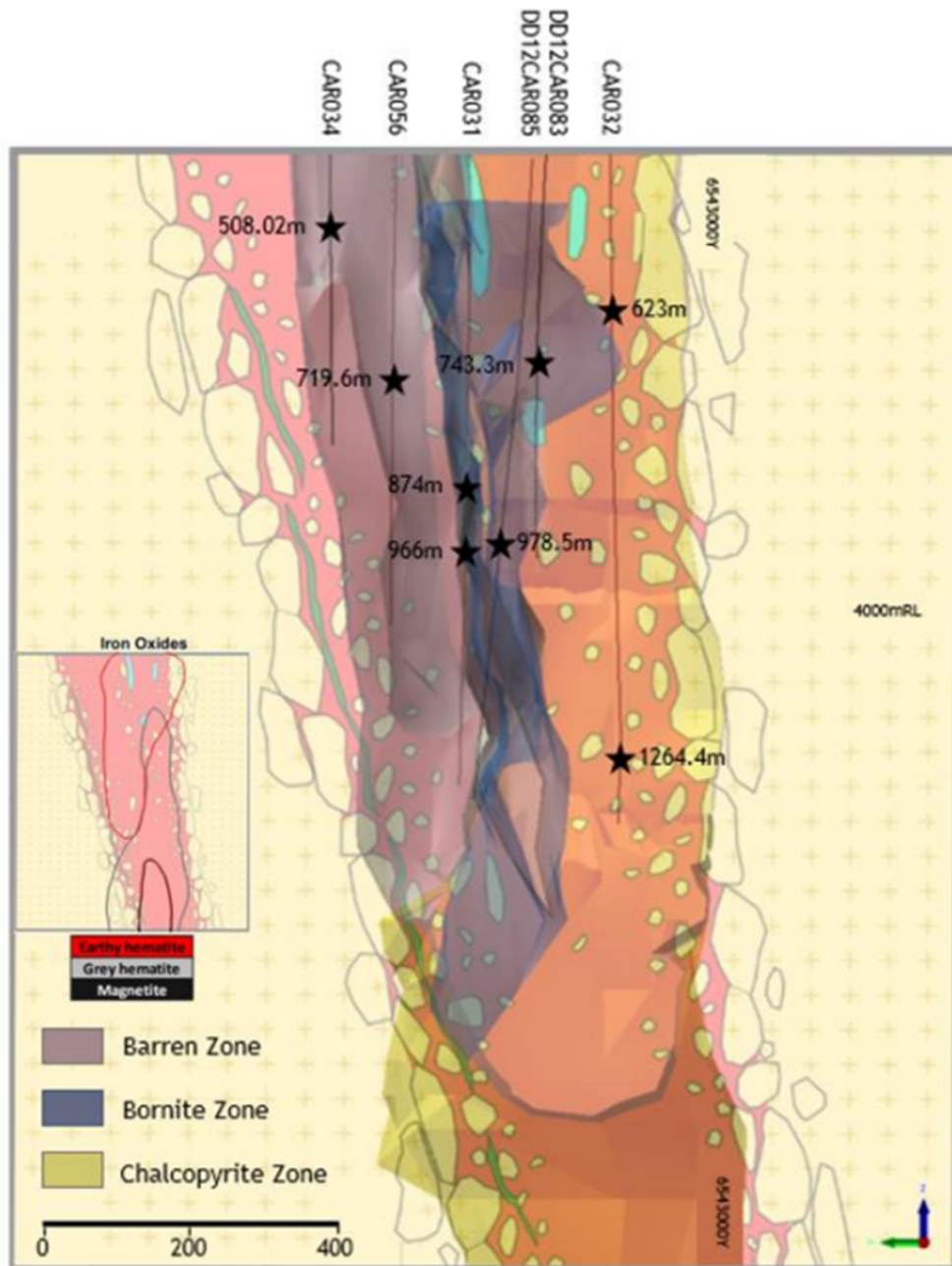
Built from the nominated geochemical data from CAR2038 and distal drillholes surrounding Carrapateena, the following granite classification plot shows an average composition of granodiorite with variation across granites to syenites.



Appendix K: Brooke Norths sample locations

Of note that the 978.5m sample is interpreted to have come from a granite raft supported by the hematite ore system.

Brooke North  
REE Minerals at Carrapateena



## Appendix- Summary Table of Utilised Samples (Methods 3.1)

Multiple Sample	Hole ID	Depth (m)	Lithology	Applications	Sample Description
	EG20CAR2038	1.6-1.8m	Granite	<b>SEM, AMICS LA_ICPMS,</b> Geochem-trends	Minor calcite and quartz veining
	EG20CAR2038	50.1	Granite	Geochem-trends	Minor calcite quartz and hematite veining
	EG20CAR2038	101.4	Granite	Geochem-trends	Fractured sample,
	EG20CAR2038	149.6	Granite	Geochem-trends	Minore hematite and quartz veining
	EG20CAR2038	196	Granite	Geochem-trends	Weak alteration (sericite)
	EG20CAR2038	249.9	Granite	Geochem-trends	Weak sericite alteration
<b>Alt and Veined</b>	EG20CAR2038	301.2	Granite	<b>SEM, AMICS LA_ICPMS,</b> Geochem-trends	Minor calcite veining
	EG20CAR2038	350	Granite	Geochem-trends	Minor quartz veining
	EG20CAR2038	399.0	Granite	Geochem-trends	Minor sericite in hematite vein
	EG20CAR2038	449	Granite	Geochem-trends	Hematite veining
	EG20CAR2038	500.1	Sericite chlorite granite	Geochem-trends	Little-no veining
	EG20CAR2038	549.9	Hematite altered Granite	Geochem-trends	Minore hematite and quartz veining
<b>Alt &amp; Veined</b>	EG20CAR2038	599.9	Sericite, Barite, Hematite altered Granite	<b>SEM, AMICS LA_ICPMS,</b> Geochem-trends	Significant veining of alteration minerals, Minor Calcite veins
	EG20CAR2038	650.0	Hematite altered Granite	Geochem-trends	Minor quartz veining
	EG20CAR2038	699.8	Hematite Granite	<b>SEM, AMICS LA_ICPMS,</b> Geochem-trends	Hematite very pervasive on granite
	EG20CAR2038	712.4	Granite Raft in Hematite breccia	Geochem-trends	Remnant granite in ore breccia
	EG20CAR2038	749.7	Hematite breccia	Geochem-trends	Ore zone,